Expedition UT-GOM2-2
Summary

Terrebonne Basin (Walker Ridge Block 313)

WR313 H002 (API 608124014800) and WR313 H003 (API 608124014900)

30 July–28 September 2023

Expedition UT-GOM2-2 Scientists

Publisher's notes

This work was supported by the U.S. Department of Energy (DOE), National Energy Technology Laboratory (NETL), under Contract No. DE-FE00223919.

This work was the result of scientific collaboration between the following institutions The University of Texas at Austin (UT), DOE, NETL, the United States Geological Survey (USGS), the Bureau of Ocean Energy Management (BOEM), The Ohio State University, Columbia University, University of New Hampshire, Oregon State University, University of Washington, Tufts University, Colorado School of Mines, and Geotek Ltd.

Disclaimer

Authorship and citation

Peter B. Flemings, Carla Thomas, Stephen C. Phillips, Timothy S. Collett, Ann E. Cook, Evan Solomon, Frederick S. Colwell, Joel E. Johnson, David Awwiller, Irita Aylward, Athma R. Bhandari, Donald Brooks, Jessica Z. Buser-Young, Alejandro Cardona, Michael A. Casso, Rachel Coyte, Tom Darrah, Marcy Davis, Brandon Dugan, Dan Duncan, John T. Germaine, Melanie Holland, Jesse Houghton, Saffron Martin, N. Tanner Mills, Michael Mimitz, Daniel Minarich, Yuki Morono, Zachary Murphy, Joshua O'Connell, Ethan Petrou, Tom Pettigrew, John W. Pohlman, Alexey Portnov, Marcie Purkey Phillips, Thomas Redd, Derek E. Sawyer, Peter Schultheiss, Kelly Shannon, Camille Sullivan, Cathal Small, Kayla Tozier, Man-Yin Tsang, Camila Van Der Maal, William F. Waite, Taylor Walton, 2025, Expedition UT-GOM2-2 Summary. In Flemings et. al., Proceedings of the UT-GOM2-2 Deepwater Hydrate Coring Expedition, University of Texas Institute for Geophysics, **https://doi.org/10.5281/zenodo.13971076**.

Copies of these proceedings can be found on OTSI.gov (**Search for UT-GOM2-2 | OSTI.GOV**), Zenodo.org (**Search Terrebonne Basin Deepwater Hydrate Coring**), and the UT-GOM2-2 website (**UT-GOM2-2: Deepwater Hydrate Coring Expedition - UT Institute for Geophysics**).

Cover photos

Left: Science party member Steve Phillips of the U.S. Geological Survey degassing pressure cores — a process that measures how much gas is in each core sample. Credit: Jackson School of Geosciences

Right: The Helix *Q4000* deepwater well intervention vessel and the 290-foot *Harvey Hermes* supply boat, carrying UT-GOM2-2 labs, pipe, fluids, and equipment, during a rendezvous on site. Photo credit: Peter B. Flemings

The Ohio State University professor Ann E. Cook talks science with The University of Texas at Austin student Ethan Petrou on the Helix *Q4000* helipad. Photo credit: Peter B. Flemings

Abstract

In the summer and fall of 2023, the University of Texas (UT) Deepwater Hydrate Coring Expedition (UT-GOM2-2) drilled, cored, made downhole measurements, and analyzed samples from the seafloor to the base of the gas hydrate stability zone at Site H, in the Walker Ridge Protracted Area Block 313 (Site H, WR313), in the Terrebonne Basin, deepwater Gulf of America (Gulf of Mexico).

Analyses of data and samples from the expedition will inform biological, geochemical, and geomechanical models to constrain the role of gas hydrates in the carbon cycle and the potential for gas hydrates as an energy resource. Pressure and conventional cores were collected continuously to a depth of 155.1 meters below the seafloor (mbsf). At deeper depths, cores were taken periodically from hydrate-bearing sands and their bounding muds to a total depth of 861.3 mbsf. 162.6 m of conventional core and 54.8 m of pressure core were recovered.

Twelve temperature measurements were made between 27.1 and 144.5 mbsf to determine the geothermal gradient. At the seafloor, more than 4 m of sandy silt of unknown origin was encountered. Beneath this sand, to a depth of about 200 mbsf, the section was composed of interbedded mud and biogenic carbonate ooze. The ooze correlated to low density and high porosity intervals observed in the previously acquired logging while drilling (LWD) data and as measured. These ooze intervals also correspond to lighter sediment color, increased Ca content based on X-ray florescence (XRF) core scanning, and increased calcareous nannofossil abundance. Calcareous nannofossil biostratigraphy constrains the entire record to the Pleistocene (< 0.91 million years),

with a pronounced increase in sedimentation rate with depth. Below 200 mbsf, the section was predominantly composed of mud with two thicker, hydrate-bearing coarse-grained intervals, which are commonly known as the Blue and Orange sands.

The dissolved gas concentration was quantified from pressure cores. In the shallow section, dissolved methane concentration increased below the sulfate-methane transition zone (SMTZ) and reaches saturation (the limit of solubility for methane) at 147 mbsf. Gas expansion was very common in conventional and depressurized pressure (conventionalized) cores below the SMTZ.

At deeper depths, the methane concentration within muds bounding the Blue and Orange reservoirs was generally found to be less than saturation. The dissolved and hydrate gas composition is consistent with a microbial source, containing greater than 99.99% methane and only trace concentrations of ethane, propane, and butane. The methane to ethane ratio (C_1/C_2) and the methane to ethane plus propane ($C_1/(C_2+C_3)$) decrease with depth down to at least 678 mbsf, mainly driven by the increase in ethane with depth. It is unclear if this trend continues through the Orange sand interval. The $\delta^{13}C$ isotopic signature of methane ranges between -69.9 and -78.5 ‰ relative to the Vienna Pee Dee Belemnite (VPDB) standard.

Pressure core recovery in sandy intervals was poor. However, pressure core logs of the Orange sand show intervals of low density and high velocity, which are indicative of high hydrate saturation. One pressure core was degassed and the average hydrate saturation in the core was determined to be 24%. One core from within the Orange sand was composed of interbedded graded sandy silt and mud. The sandy silts from this core are composed of mainly quartz and feldspar with some lithics. Most of the recovered pressure core samples are maintained at near in-situ pressure and temperature (within the hydrate stability field) at the University of Texas Pressure Core Center awaiting analysis.

In the shallow section, samples will be used to determine the flux of organic carbon through the basin system, find the rate at which that carbon was consumed, and understand the microbial population responsible for these processes. In the deeper section, samples from in and around the hydrate reservoirs will be used to determine the petrophysical properties of the reservoir and bounding seals in these systems.

https://doi.org/10.5281/zenodo.13971076

Table of contents

List of figures

 https://doi.org/10.5281/zenodo.13971076

List of tables

List of equations

Note

Expedition results are detailed in Expedition UT-GOM2-2 Site H (Flemings et al., **2025a**). Methods are described in the Expedition UT-GOM2-2 Methods (Flemings et al., **2025b**). Lists of all acronyms, abbreviations, symbols, units, conversion factors, and sample codes used in these proceedings are also provided in Methods (Flemings et al., **2025b**).

Members of the science party arrive via helicopter on site at Walker Ridge Block 313. Photo credit: Geotek Ltd.

Introduction

In the summer and fall of 2023, the University of Texas (UT) Deepwater Hydrate Coring Expedition (UT-GOM2-2) drilled, cored, made downhole measurements, and analyzed samples from the seafloor to the base of the gas hydrate stability zone at Site H in the Walker Ridge Protracted Area Block 313 (Site H, WR313) in the Terrebonne basin, deepwater Gulf of America (Gulf of Mexico), herein the Gulf.

This was the primary expedition of the Deepwater Methane Hydrate Characterization & Scientific Assessment project (DE-FE0023919). This project is funded by the United States Department of Energy (DOE), National Energy Technology Laboratory (NETL), and advised by the United States Geological Survey (USGS) and the Bureau of Ocean Energy Management (BOEM). We successfully sampled and analyzed the physical, chemical, and biological properties of hydrate-bearing reservoirs, their bounding strata, and the overlying sedimentary section. Completed and ongoing analyses of data and samples from the expedition will inform biological, geochemical, and geomechanical models to constrain the role of gas hydrates in the carbon cycle and the potential for gas hydrates as an energy resource.

The program planned to recover samples from the first few hundred meters beneath the seafloor to illuminate the microbial factory that is the primary source of the methane found in gas hydrates in the deep oceans. We sought to determine the flux of organic carbon through the basin system, find the rate at which that carbon was consumed, and methane was produced, and understand the microbial population responsible for these processes. We also sampled deeper, hydrate-bearing reservoirs, and their bounding non-reservoir units to interpret the petrophysical properties of these reservoirs and illuminate the mechanisms by which they formed.

We first summarize the underlying scientific questions that drove the program. We then provide a geological overview of the study region. We then integrate our understanding of the geologic framework of the study area with the scientific questions to be addressed to develop the expedition operational plan. We then summarize the execution of the drilling and core analysis program. This includes an overview of the execution, the drilling operations, and a summary of scientific results.

 https://doi.org/10.5281/zenodo.13971076

Geotek Ltd. team members onboard the *Q4000*. team Photo credit: Peter B. Flemings

Scientific motivation

Approximately 10,000 billion tons of mobile carbon (in land plants, peat, soil, organic and inorganic carbon dissolved in the ocean, and fossil fuels) constantly cycle through the solid Earth, the ocean, and the atmosphere (Isson et al., **2020**; You et al., **2019**). Of this carbon, 5-22% is trapped in gas hydrate, an ice-like substance composed mostly of methane and water (Boswell and Collett, **2011**; Milkov, **2004**; Ruppel and Kessler, **2017**; Sloan and Koh, **2007**).

Most of this massive carbon reservoir lies in continental marine margin sediments within a layer that extends downward from the seafloor and can reach thicknesses of ~1,000 m (3,280 ft.) (Boswell and Collett, **2011**; Kvenvolden, **2012**). This layer interacts with the Earth's ocean and, perhaps, the atmosphere (Ruppel and Kessler, **2017**). This dynamic carbon reservoir is a potential energy resource (Boswell and Collett, **2011**), a potential source of geohazards (Kayen and Lee, **1991**; Mienert et al., **2005**), and a potential driver for climate change (Kennett et al., **2000**; Ruppel and Kessler, **2017**).

Gas hydrates, the global carbon cycle, and the microbial factory

The atmosphere currently contains only 8% (~800 billion tons) of the total mobile carbon (Schuur et al., **2008**). Thus, the hydrate carbon reservoir is of the same scale as that of the atmosphere. Furthermore, methane is a greenhouse gas with 84 times the radiative forcing of carbon dioxide (CO_2) over a 20-year timeframe (Ruppel and Kessler, **2017**), any leakage of methane directly into the atmosphere can disproportionately impact climate. However, current evidence suggests that methane seeping from the seafloor within the hydrate stability zone is unlikely to pass through the ocean to reach the atmosphere (Ruppel and Kessler, **2017**). Instead, in many locations above hydrate deposits, methane vents into the overlying ocean and it is commonly oxidized, resulting in potential ocean acidification (Biastoch et al., **2011**; Boudreau et al., **2015**). In addition, methane flowing

upward within seafloor sediments is largely oxidized within near-seafloor sediments, leading to a flux of dissolved carbon into the ocean (Reeburgh, 2007). However, large-scale hydrate dissociation events and the consequent methane emissions have been proposed to cause large climate perturbation in the geologic past (Dickens, 2003; Kennett et al., 2000; Ruppel and Kessler, 2017). However, the workings of this sedimentary carbon recycling factory and the role played by gas hydrates are not yet completely understood. A detailed sampling program of the marine water column and the underlying subsea sedimentary section has the potential to better illuminate these fluxes in the marine hydrate system.

At the root of this system is the microbial factory that ultimately produces methane (Claypool and Kaplan, 1974; Kayen and Lee, 1991; Kvenvolden, 1988; Mienert et al., 2005). Wei et al. (2024) review the complex process by which primary organic carbon in marine sediments is broken down by a sequence of microbially-mediated reactions to generate dissolved organic carbon of decreasing molecular weights, which are eventually utilized in terminal respiratory processes such as methanogenesis.

We are only beginning to explore the microbial communities that are present, and the complex interactions and kinetics that control this process. A detailed sampling program of geochemistry and microbiology as a function of depth of burial has the potential to further illuminate these processes.

Gas hydrates and energy

The large amount of natural gas stored in gas hydrates makes hydrate reservoirs one of the most abundant possible unconventional energy resources on Earth (Boswell and Collett, 2011; Milkov, 2004; Yin and Linga, 2019). Most of these hydrates lie within mudrocks and are unlikely to be of economic value because they have low hydrate concentration and little permeability (Boswell, 2009; Milkov, 2004). In contrast, Japanese researchers found hydrate saturations greater than 80% in silts and sands of the Nankai Trough (Tsuji et al., 2004). The high hydrate saturation and high intrinsic permeability of these deposits make them attractive for energy production (Boswell, 2009; Boswell and Collett, 2011).

These types of hydrate reservoirs have now been found around the globe and recent expeditions have focused on characterizing their petrophysical behavior (You et al., 2021; You and Flemings, 2021). This work has focused on illuminating the effective permeability and the geomechanical behavior of the hydrate-bearing reservoirs and their bounding non-reservoir sections (Biastoch et al., 2011; Boudreau et al., 2015).

An accurate description of petrophysical behavior will better constrain reservoir simulation models and allow us to evaluate optimal approaches to safely produce hydrate reservoirs (Boswell et al., 2019). The chemistry and methane concentration of these reservoirs and their bounding seals can also be used to test models by which these reservoirs formed.

A central challenge has been to understand the mechanism by which coarse grained hydrate reservoirs are charged and established through time (Malinverno and Goldberg, 2015). This will strengthen our ability to explore for hydrate reservoirs.

Gas hydrate and CO_2 sequestration

CO_2 could be stored as an immobile, solid, CO_2-hydrate. One strategy that has been attempted is to replace methane in a hydrate reservoir with CO_2 (Boswell et al., 2017), preserving the reservoir's geomechanical stability and reducing the environmental impact of the produced methane.

An alternative approach is to inject CO_2 into an aquifer that lies within the hydrate stability zone (Bhati et al., 2024; Darnell et al., 2019; Zheng et al., 2020). An improved understanding of the thermodynamic behavior of multi-component systems and of the geomechanical properties of gas hydrate reservoirs will inform simulation models for CO_2 sequestration that seek to optimize storage approaches (Zhang et al., 2011).

https://doi.org/10.5281/zenodo.13971076

Oregon State professor and lead microbiologist Rick Colwell places microbiology samples in the -80 °C freezer.
Photo Credit: Jackson School of Geosciences

Background

UT-GOM2-2 drilled and cored two boreholes at Site H WR313 (Figure F1). Site H was originally drilled (Hole H001) using logging while drilling (LWD) during the 2009 Gas Hydrates Joint Industry Project Leg II (JIP II) (Boswell et al., 2012a; Boswell et al., 2012b; Frye et al., 2012; Hutchinson et al., 2008; Shedd et al., 2010).

Geological overview

The study area is located near the southern boundary of Terrebonne Basin, in WR313, about 193 miles (168 nautical miles) southwest of Port Fourchon, Louisiana, USA (Figure F1). The water depths range from 6,000 ft to 6,800 ft in the study area (Figure F2). The local seafloor topographic gradient in the study area varies between 2° and 3°.

Terrebonne Basin is a salt-floored and salt-bounded mini-basin on the midslope of the central deepwater Gulf (Diegel et al., 1995; Frye et al., 2012; Prather et al., 1998). The strata that infill the basin dip and thicken to the north (Figure F3). Portnov et al. (2023) and Varona et al. (2023) describe the regional stratigraphy of the basin sediments.

McConnell and Kendall (2002) first identified and described gas hydrate potential in the southeastern lobe of the Terrebonne Basin, where they observed seismic discontinuities called bottom simulating reflections (BSRs)

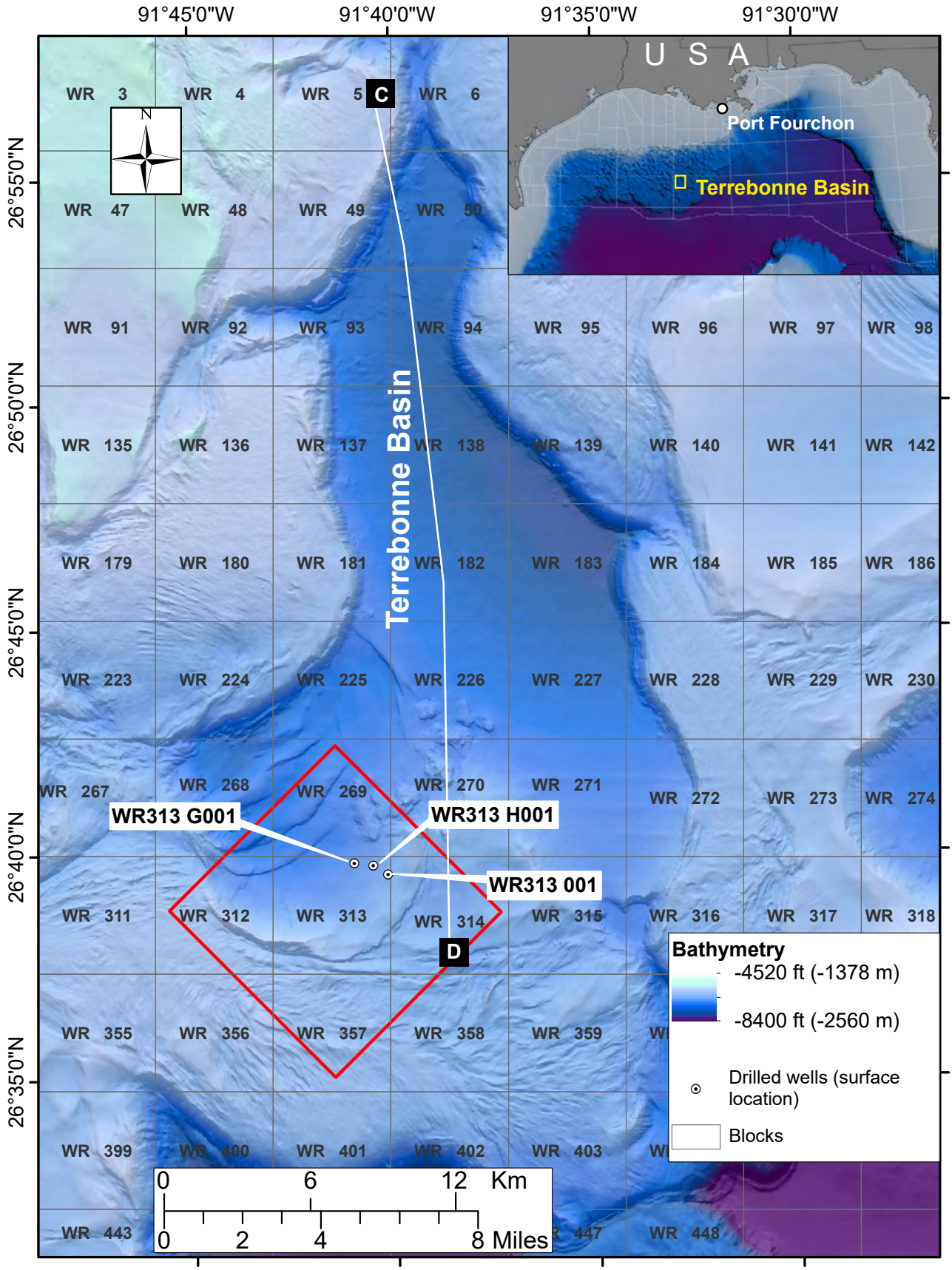

Figure F1: Seafloor shaded relief map of the northwest (NW) part of the Walker Ridge (WR) Protraction Area showing Terrebonne Basin and previously drilled locations in Walker Ridge Block 313 (WR313). The inset map shows the position of Terrebonne Basin. The red box highlights the study area and is expanded in Figure F2. The transect between "C" and "D" is illustrated in Figure F3. The bathymetry data are from the U.S. Bureau of Ocean Energy Management (BOEM) Northern Gulf Deepwater Bathymetry Grid from 3D Seismic (Kramer and Shedd, 2017).

https://doi.org/10.5281/zenodo.13971076

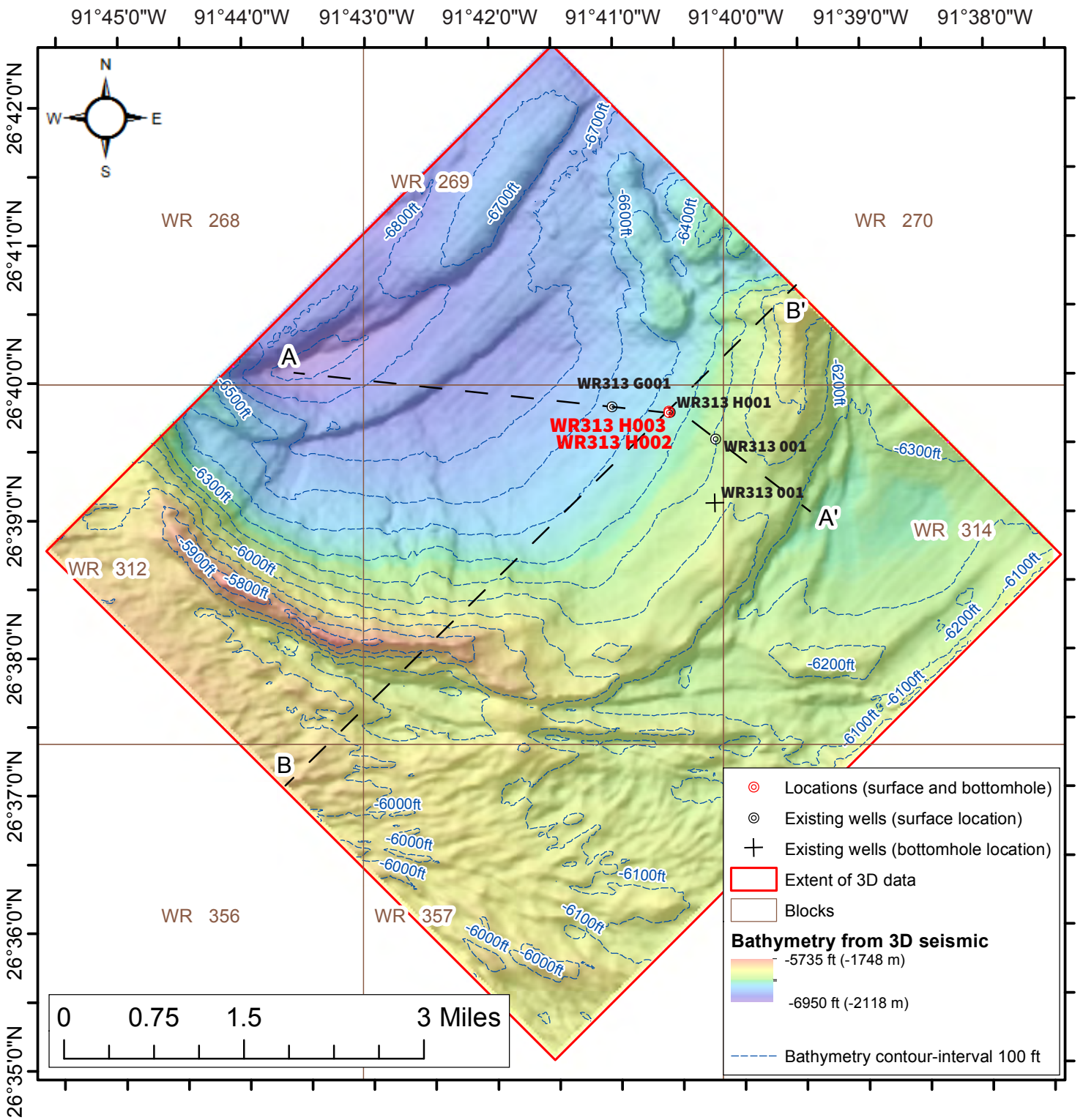

Figure F2: Bathymetry map of the study area in the southern Terrebonne Basin, showing the locations of boreholes drilled prior to and during this expedition. Previously drilled boreholes are shown with black labels. Walker Ridge Block 313 (WR313) H002 (Hole H002) and WR313 H003 (Hole H003), shown with red labels, were drilled during this expedition. The transect between "A" and "A'" is presented in Figure F4. The transect between "B" and "B'" is presented in Figure F5. Bathymetry is based on three-dimensional (3D) seismic data, courtesy of WesternGeco.

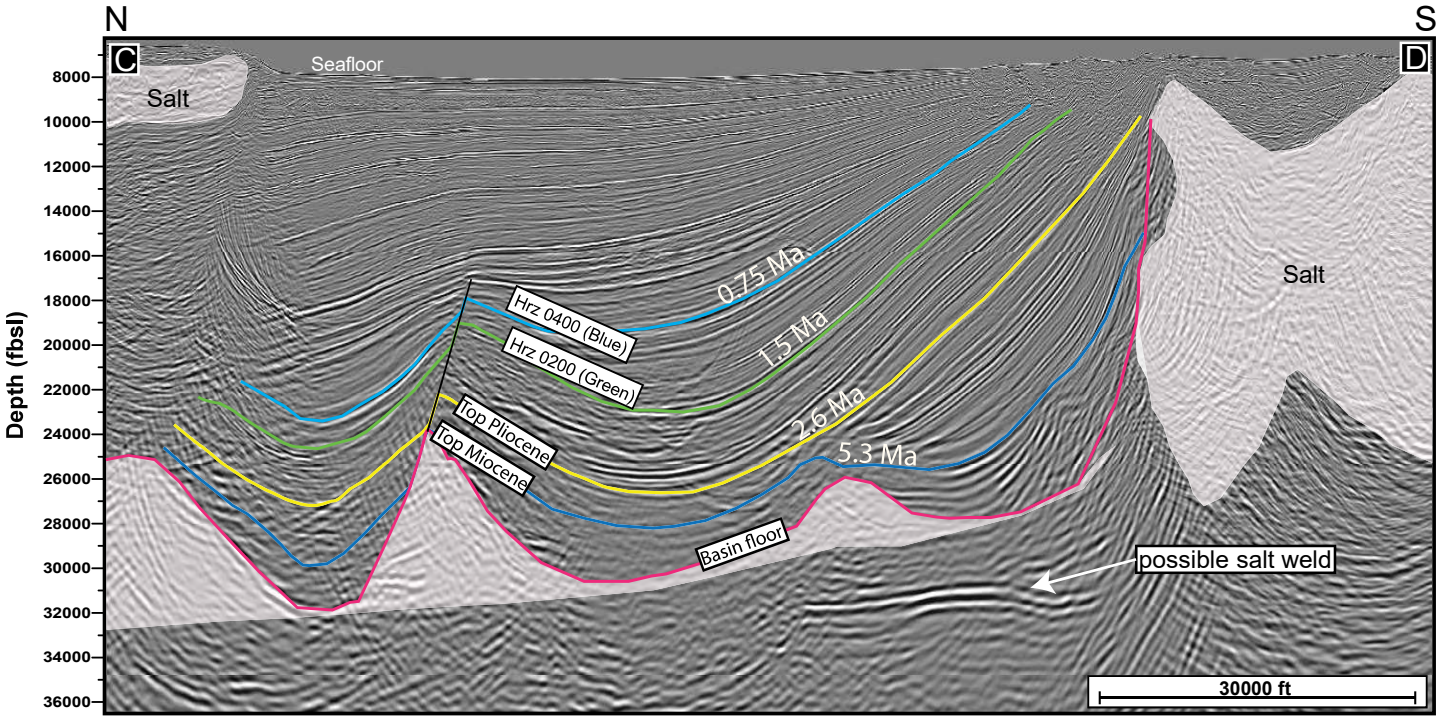

Figure F3: North-South regional cross section through the Terrebonne Basin (located in Figure F1). The interpreted ages are based on existing calcareous nannofossil and foraminifera biostratigraphy data from industry wells as described by Portnov et al. (2023). Figure modified from Portnov et al. (2023).

that they interpreted to record the base of hydrate stability zone (BHSZ) (Frye et al., 2012; McConnell and Kendall, 2002) (Figures F4 and F5).

The BHSZ marks the boundary above which hydrate is stable and below which hydrate is not stable. At WR313, the presence of high saturation hydrate in coarse-grained layers results in a high acoustic impedance or positive polarity reflection due to the high velocity of the hydrate (Boswell et al., 2016; McConnell and Zhang, 2005). Below the base of hydrate stability, gas may be present, causing a decrease in velocity and a significant negative acoustic impedance or negative polarity reflection. Thus, within a single horizon, the change in acoustic impedance from positive polarity reflection (peak) to a negative polarity reflection (trough) can be mapped as the BHSZ (Hillman et al., 2017b; McConnell and Kendall, 2002; Portnov et al., 2023; Shedd et al., 2012).

Three previously-drilled boreholes exist in the WR313 study area (Figure F1; Tables T1 and T2). One exploration well, WR313 001, was drilled by Devon Energy in 2001 to target Pliocene and Miocene oil reservoirs (Figure F1). Two LWD boreholes WR313 G001 (Hole G001) and WR313 H001 (Hole H001) (Figure F1), were drilled during JIP II to test gas hydrate targets (Boswell et al., 2012a; Boswell et al., 2012b; Collett et al., 2009; Frye et al., 2012; Hutchinson et al., 2008; Shedd et al., 2010).

Seismic horizons were mapped on 3D seismic data throughout the study area and assigned a numerical designation for each mapped horizon with the numbering increasing upward (e.g. Figure F4). Mapped horizons correlate to previously mapped horizons by others but they used a different nomenclature (Boswell et al., 2012a; Boswell et al., 2012b; Hillman et al., 2017b).

For example, Horizon (Hrz) 0300 is a seismic reflection that correlates with the top of the Orange sand interval. This horizon was previously termed the Orange horizon. It is thus presented as Hrz 0300 (Orange) in this study (e.g. Figure F4). Similarly, Horizon 0400 is a regionally mappable reflector associated with the top of the lower Blue sand and is termed Hrz 0400 (Blue). Hrz 0300 (Orange) and Hrz 0400 (Blue) are prominent reflectors in the 3D seismic

https://doi.org/10.5281/zenodo.13971076

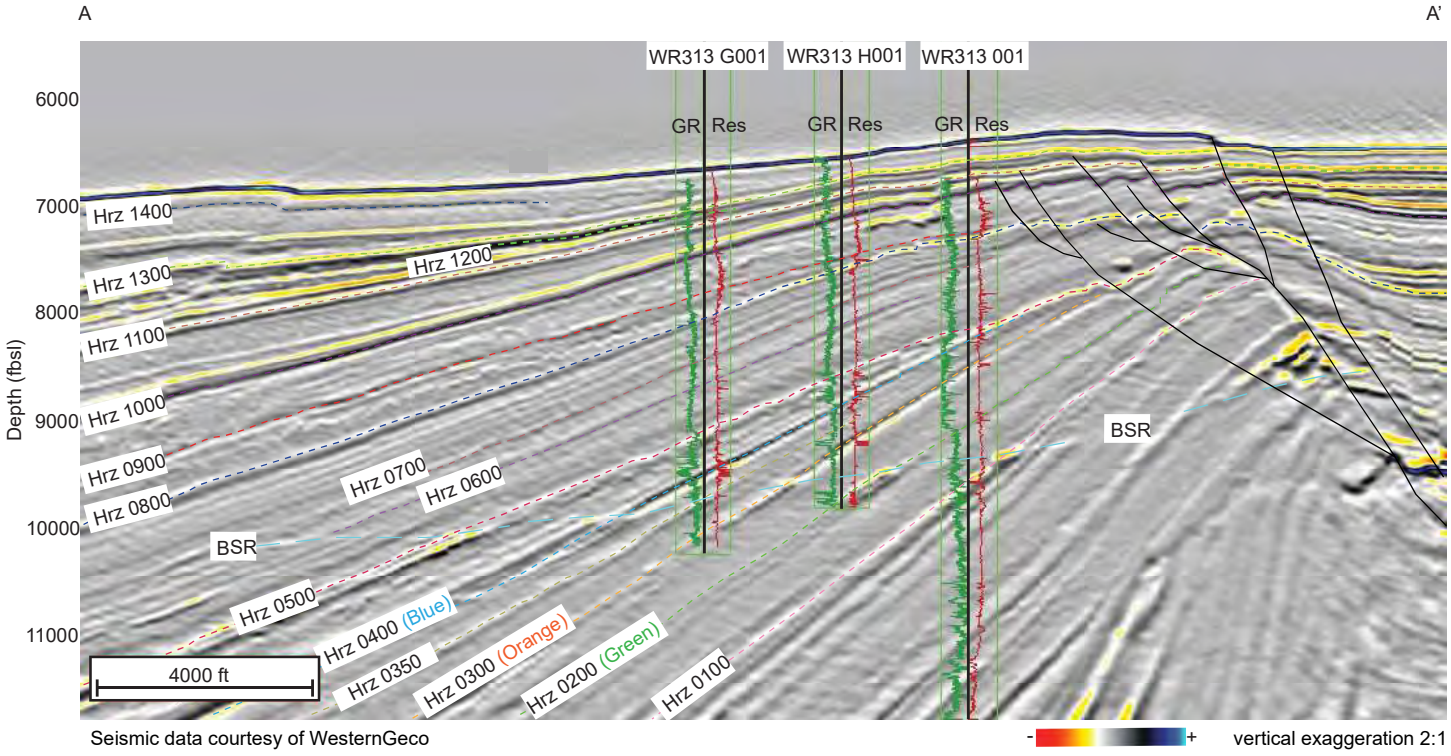

Figure F4: Seismic section A to A' through previously drilled boreholes in Walker Ridge Block 313 (WR313) (located in Figure F1). Seismic horizon (Hrz) nomenclature used in this study is delineated as 'Hrz #'. Previous nomenclature is shown in parenthesis (Boswell et al., 2012b; Frye et al., 2012; Hillman et al., 2017a). The connected bottom simulating reflections (BSR), and logging while drilling (LWD) gamma ray (GR) and LWD resistivity (Res) logs of the previously drilled holes are also shown with values increasing to the right. Seismic data courtesy of WesternGeco.

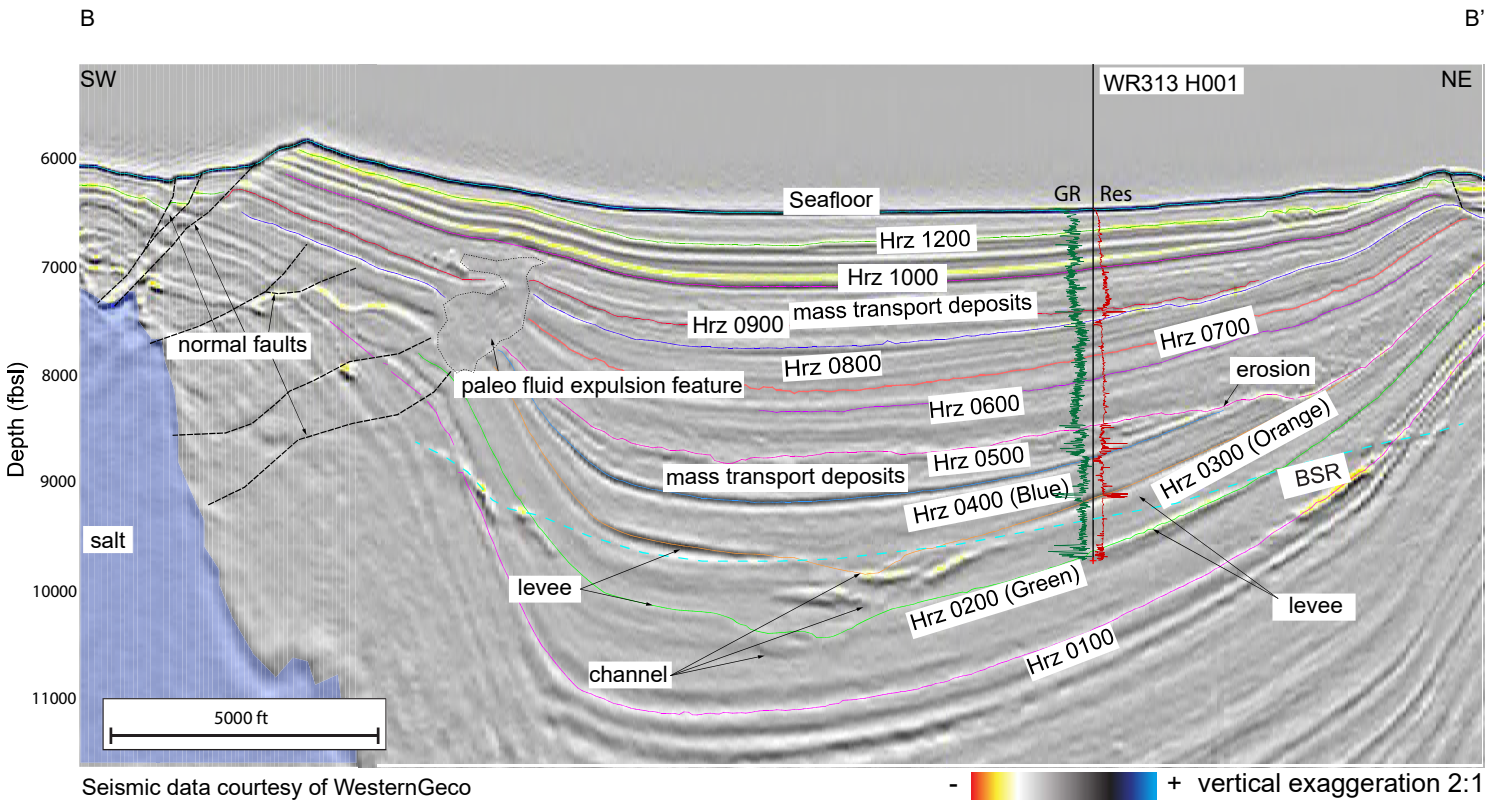

Figure F5: Southwest (SW) to northeast (NE) oriented seismic section B to B' (located in Figure F2) through Hole H001 showing major seismic features in the study area. Logging while drilling (LWD) Resistivity (RES) and gamma ray (GR) logs are shown at Hole H001 with values increasing to the right. Seismic data courtesy of WesternGeco.

Borehole	API Number	Surface Lat. (NAD27)	Surface Long. (NAD27)	Bottom Lat. (NAD27)	Bottom Long. (NAD27)
WR313 001	608124000700	26° 39' 32.83''	-91° 40' 11.66''	26° 39' 04.66''	-91° 40' 12.31''
WR313 G001	608124003900	26° 39' 47.48''	-91° 41' 01.94''	26° 39' 47.91''	-91° 41' 01.81''
WR313 H001	608124004000	26° 39' 44.85''	-91° 40' 33.75''	26° 39' 44.99''	-91° 40' 33.18''

Table T1: Surface and bottom-hole locations of previously drilled boreholes in WR313 (BSEE, 2024). API = American Petroleum Institute; NAD27 = North American Datum of 1927; WR313 = Walker Ridge Block 313; BSEE = U.S. Bureau of Safety and Environmental Enforcement

Borehole	API Number	Total MD (ft RKB)	TVD (ft RKB)	Air Gap (ft)	Water Depth (ft)
WR313 001	608124000700	16,720	16,072	72	6,216
WR313 G001	608124003900	10,200	10,199	52	6,562
WR313 H001	608124004000	9,888	9,887	51	6,462

Table T2: Total Depth, rig height (air gap), and water depth of previously drilled boreholes in WR313 (BSEE, 2024). API = American Petroleum Institute; MD = Measured Depth; TVD = Total Vertical Depth; WR313 = Walker Ridge Block 313; BSEE = U.S. Bureau of Safety and Environmental Enforcement

data and display a distinct phase reversal when they intersect the local BSR.

This phenomenon, described above, guided the project seismic mapping strategy. Each of these seismic horizons were traced as a seismic peak above the BSR and as a seismic trough below the BSR (Boswell et al. (2012b) for an explanation of mapping strategy). In addition to the seismic horizons, a horizon was also generated connecting the discontinuous but locally strong BSR (Figure F4).

Hole G001, Hole H001, and WR313 001 penetrate Hrz 0400 (Blue) above the BSR (Figure F6), whereas only Hole H001 and WR313 001 penetrate Hrz 0300 (Orange) above the BSR (Figure F7). These wells confirmed that positive seismic amplitudes above the base of hydrate stability record the presence of hydrates. Hole G001 penetrated Hrz 0300 (Orange) below the BSR. At this location, the Orange sand was mud prone and gas was not present. Frye et al. (2012), Boswell et al. (2012b), and Varona et al. (2023) interpret the specific depositional environments of the Blue and Orange sands.

Site H seismic and LWD interpretation

In preparation for coring, LWD and seismic data were used to characterize the sediment type and hydrate occurrence at Hole H001. Five units ('LWD Units', e.g., Figure F8) were interpreted and the porosity along the borehole was calculated. Hydrate saturation within coarse-grained sediments was also calculated. Figure F9 and Figure F10 show the planned primary coring intervals: the shallow near-seafloor system (Figure F9), the Red sand (Figure F10, top), the Upper Blue sand (Figure F10, middle) and the Orange sand (Figure F10, bottom).

In LWD data, water-saturated and gas hydrate-saturated sediments have unique signals. Water-saturated, unconsolidated, coarse-grained sediments usually wash out of the borehole during drilling and coring, leading to a very low LWD resistivity (often lower than the rest of borehole), enlarged caliper measurements, low bulk density, and low gamma ray. In comparison, water-saturated marine muds usually have stable borehole size, a resistivity between 1-2 Ωm, and a mid-range gamma ray (between 60-120 API). Hydrate-saturated coarse-grained sediments have high resistivity, high P-wave velocity, little to no change in bulk density, and low gamma ray values. This set of log responses indicates that hydrate is in the primary pore space of coarse-grained sediments.

In contrast, hydrate in marine muds often forms in near vertical fractures, and these have been observed at Hole H001 (Cook et al., 2014). These intervals have high resistivity, hydrate-filled fractures visible on resistivity logs, and separation between propagation resistivity curves (Cook et al., 2010). The

https://doi.org/10.5281/zenodo.13971076

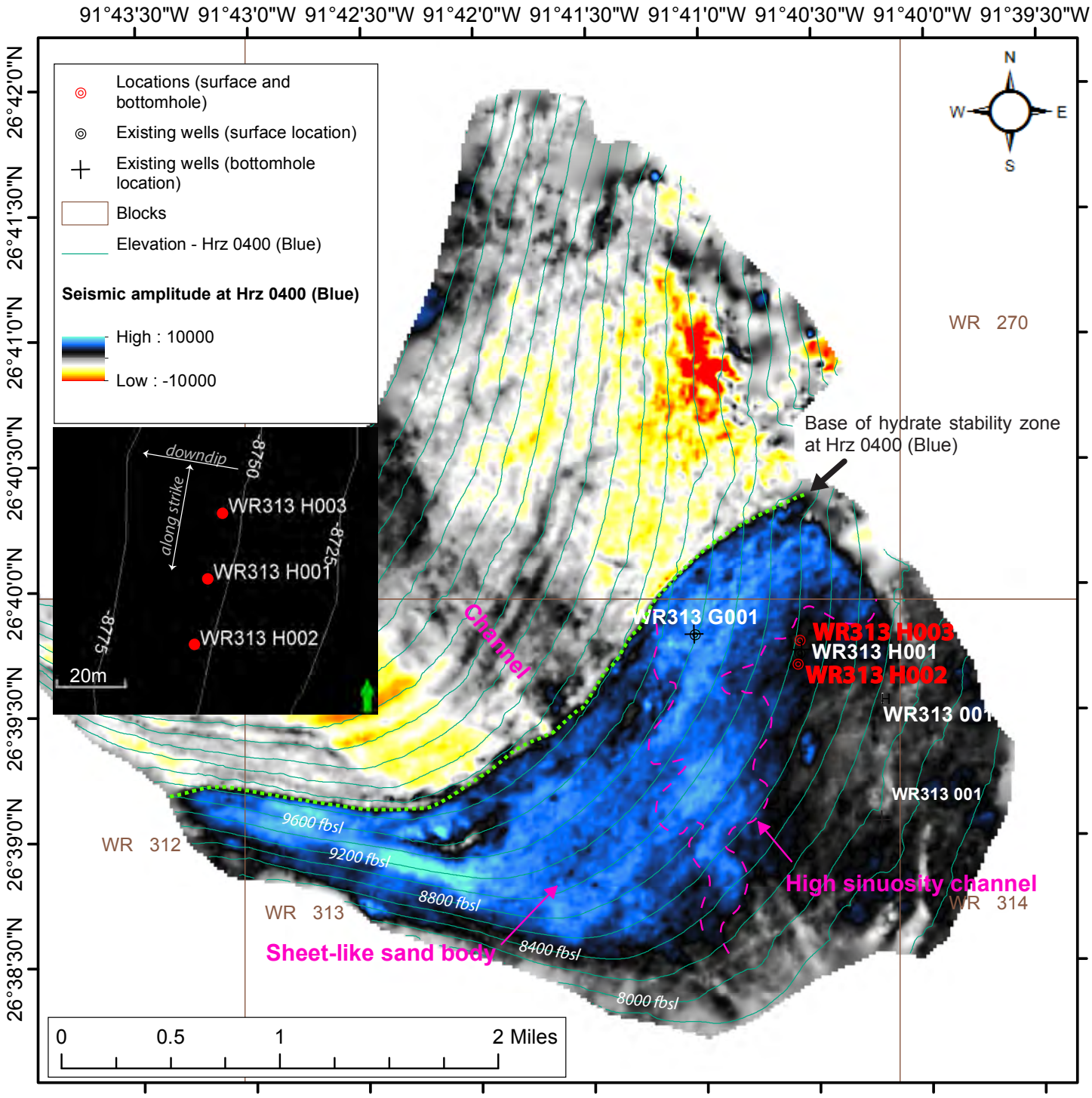

Figure F6: Instantaneous amplitude map of Horizon (Hrz) 0400 (Blue) Walker Ridge Block 313 (WR313) showing the geological interpretation of the lower part of the Blue sand interval (Boswell et al., 2012b). Inset illustrates an expanded view of the H001 showing the location of the previously drilled borehole WR313 H001 and the two proposed boreholes (WR313 H002 and WR313 H003) drilled in this study. The lower portion of the Blue sand does not extend to Hole H001. The top of the Blue sand interval (Upper Blue) was encountered in Hole H001 with a total thickness of 52 ft. Maps generated from three-dimensional (3D) seismic data used with the permission of WesternGeco.

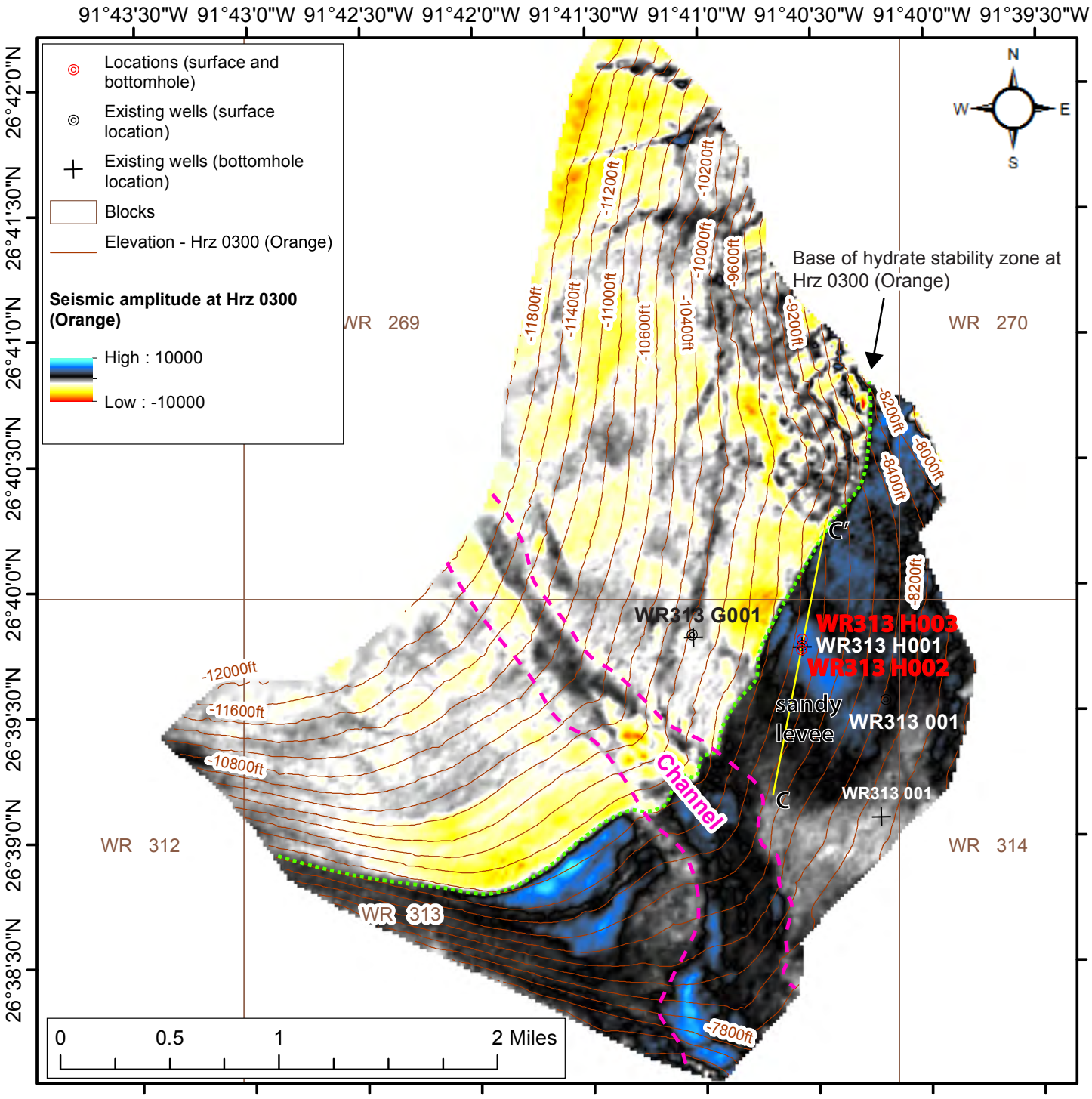

Figure F7: Instantaneous amplitude map of Horizon (Hrz) 0300 (Orange) Walker Ridge Block 313 (WR313) showing geological interpretation for the Orange sand. The previously drilled borehole WR313 H001 and the proposed boreholes WR313 H002 and WR313 H003 target gas hydrate-bearing sands showing strong positive amplitude response (blue color). Maps generated from three-dimensional (3D) seismic data used with the permission of WesternGeco.

https://doi.org/10.5281/zenodo.13971076

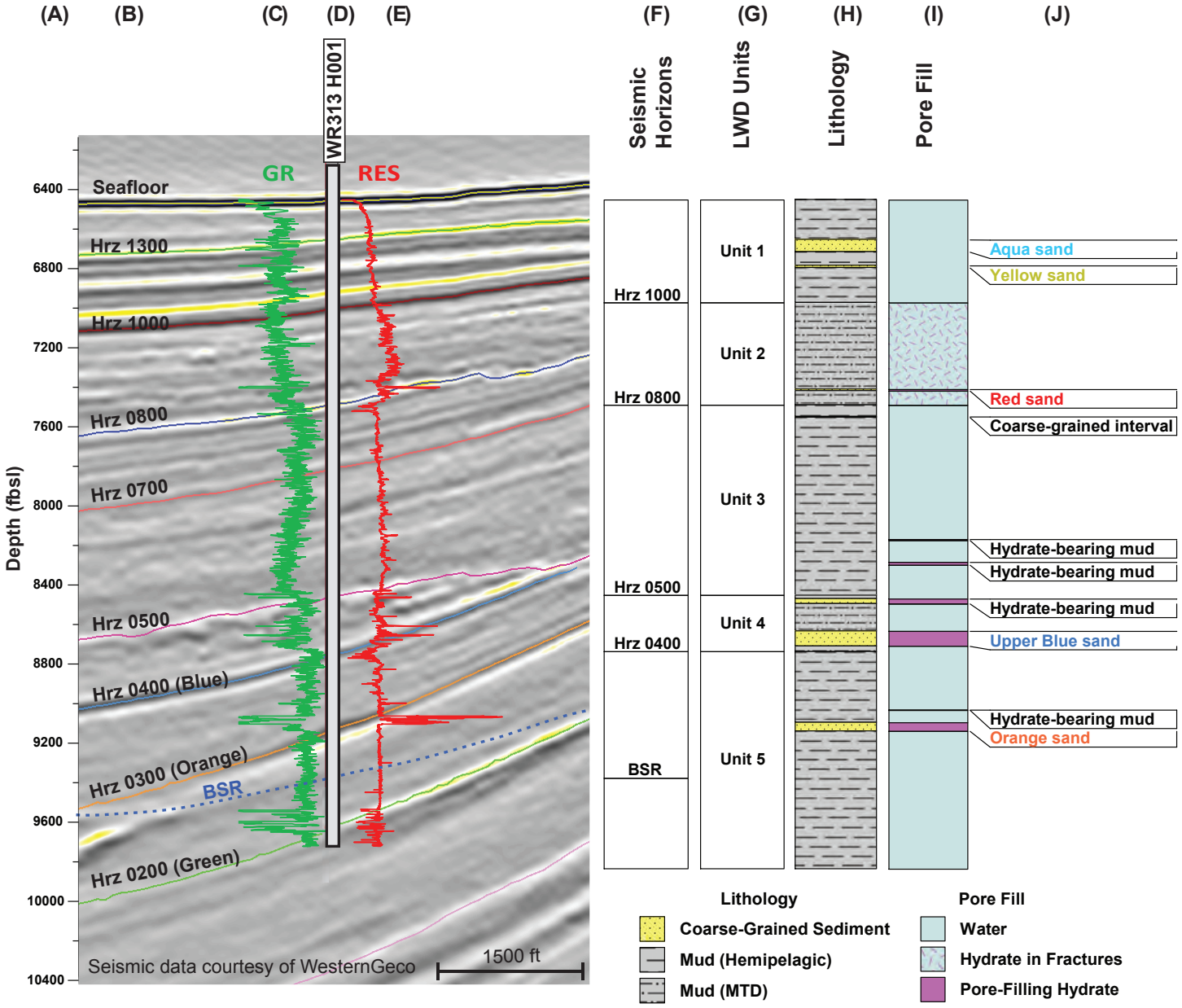

Figure F8: Stratigraphic overview of Hole H001. A) Depth in feet below sea level (fbsl); B) Seismic cross section running through Hole H001 with major seismic horizons (Hrz) labeled on the left-hand side; C) Logging while drilling (LWD) gamma ray (GR) with GR value increasing to the right; D) Location of Hole H001 on the seismic cross section; E) LWD resistivity (RES) with values increasing to the right; F) Seismic horizons (Hrz); G) LWD units and bottom simulating reflector (BSR) defined by LWD and seismic data; H) Interpreted lithology; I) Interpreted pore fill; J) Interpreted sands and other events.

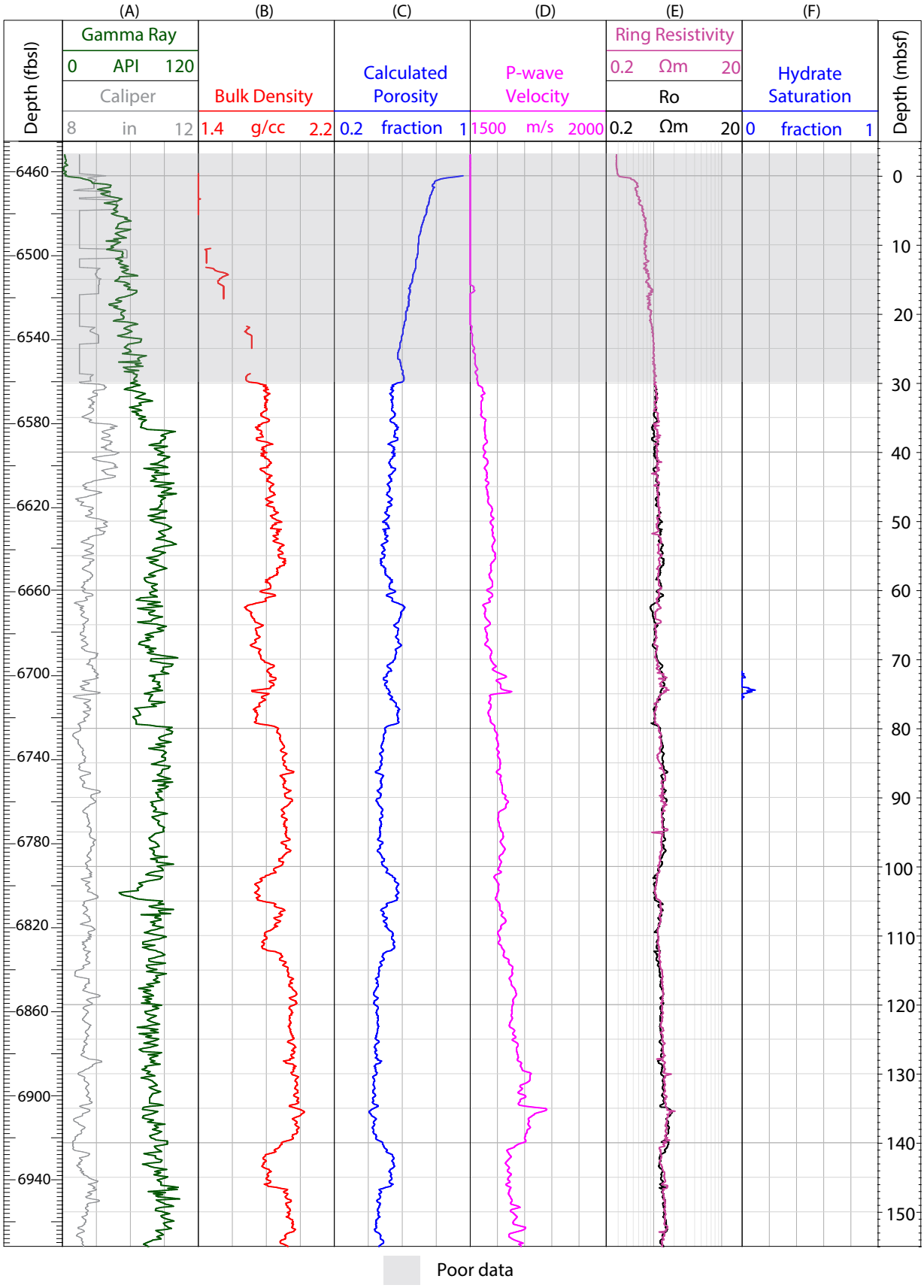

Figure F9: Hole H001 Logging while drilling (LWD) data for the uppermost interval (0-150 mbsf), LWD Unit 1 with calculated porosity and hydrate saturation. The top interval is gray because the LWD data in the near-seafloor interval are of poor quality; A) LWD gamma ray (green line) and caliper data (gray line); B) LWD bulk density (red line); C) LWD calculated porosity (blue line); D) LWD P-wave velocity (pink line); E) LWD ring resistivity (light purple line) and formation resistivity with 100% water (R_o); F) Calculated hydrate saturation (blue line).

https://doi.org/10.5281/zenodo.13971076

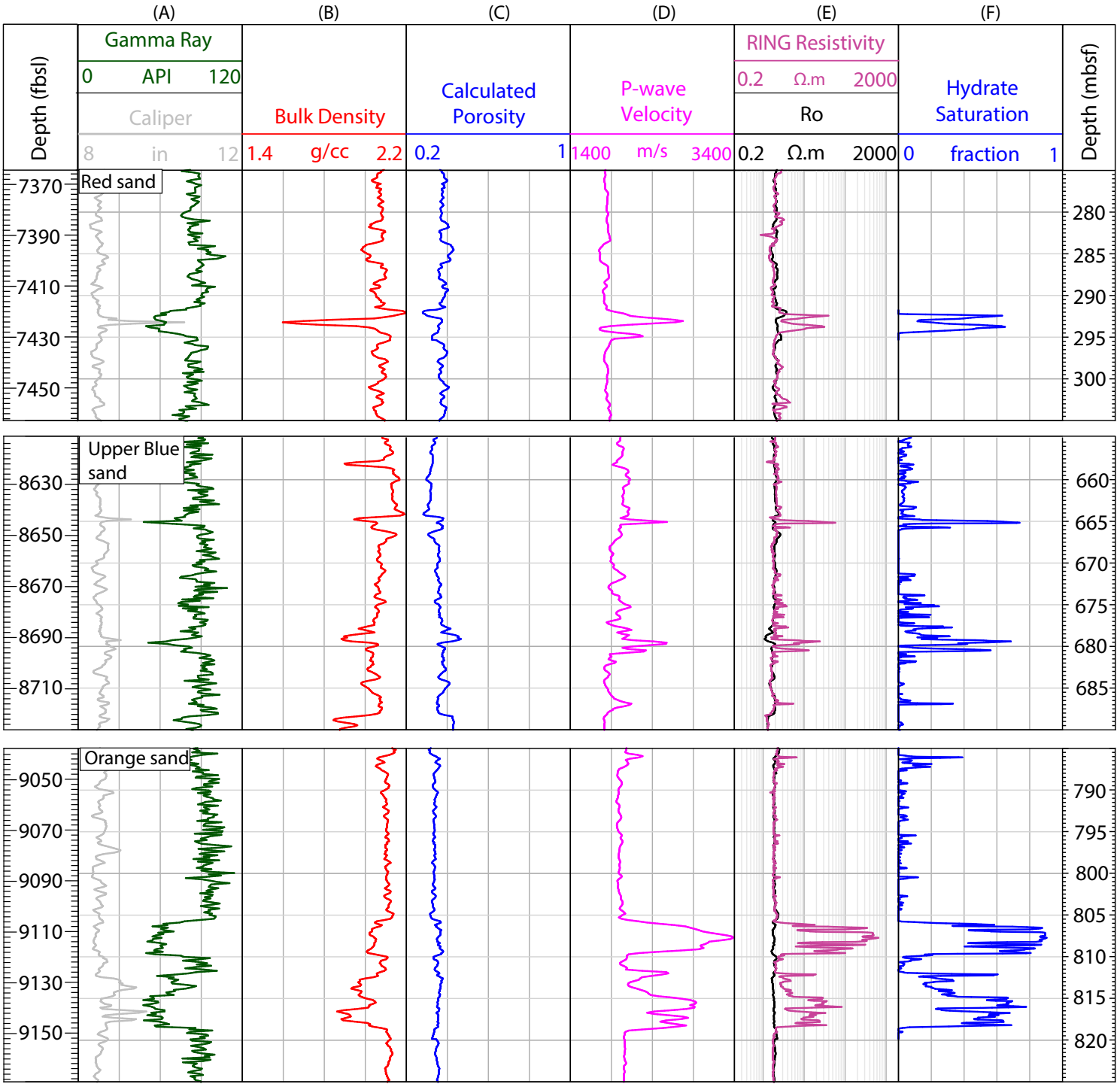

Figure F10: Hole H001 measured logging while drilling (LWD) data in sand intervals including the Red sand (LWD Unit 2), the Upper Blue sand (in LWD Unit 4), and the Orange sand (in LWD Unit 5) with calculated porosity and hydrate saturation. A) LWD gamma ray (green line) and caliper data (gray line); B) LWD bulk density (red line); C) LWD calculated porosity (blue line); D) LWD P-wave velocity (pink line); E) LWD ring resistivity (light purple line) and formation resistivity with 100% water (R_o); F) Calculated hydrate saturation (blue line).

high resistivity observed in these intervals, however, is caused by electrical anisotropy and not uniformly high hydrate saturation.

Hydrate saturation (S_h) is calculated from logging data using Archie's equation (Equation **E1**) in coarse-grained intervals only, as Archie's equation is not accurate when vertical fractures or vugs are present (Archie, **1942**; Goldberg et al., **2010**).

$$S_h = 1 - \left(\frac{R_W}{\phi^m R_{RING}} \right)^{\frac{1}{n}}$$

Equation E1.

To calculate hydrate saturation, the LWD resistivity log with the highest vertical resolution for its depth of penetration, which is ring resistivity, R_{RING} (Cook et al., **2012**) was used. Water resistivity, R_w, is calculated using Fofonoff and Millard (**1983**). The Archie tortuosity exponent, *m*, is estimated from water-saturated intervals and ranges from 1.9 to 2.5 for Hole H001. The hydrate saturation exponent, *n*, is set to 2.5 (Cook and Waite, **2018**).

Finally, the porosity, ϕ is calculated from LWD bulk density using a pore water density of 1.03 g/cm^3, a hydrate density of 0.925 g/cm^3, and grain density of 2.65 g/cm^3 for coarse-grained intervals and 2.7 g/cm^3 for muds (Figures **F9** and **F10**). These are common values used for the Gulf and are comparable to those measured for Green Canyon Block 955 (Fang et al., **2020**). In zones of borehole washout, the bulk density was very low. In these zones, the porosity was edited to reflect what was present in similar lithologies in nearby intervals.

The five LWD units defined at Hole H001 using LWD and seismic data (Figure **F8**) are as follows:

LWD Unit 1 extends from the seafloor to Hrz 1000 (0-6,982 fbsl [0-158 mbsf]). In the seismic data, LWD Unit 1 is imaged as sub-parallel reflections. The LWD data has a high gamma ray response indicating marine mud with few relatively thin lower gamma ray intervals. LWD Unit 1 is interpreted as a fine-grained hemipelagic interval with variable bulk density.

Downdip, in Hole G001, the lower-density intervals contain several cm to m-thick coarse-grained beds, identified as the Aqua and Yellow sands; however, these sands are either not present or very thin at Site H. One thin interval at 74 mbsf was identified that may be a coarse-grained hydrate bearing sand; if it contains hydrate, the hydrate saturation is low <10% (Figure **F9**).

LWD Unit 2 extends from Hrz 1000 to Hrz 0800 (6,982-7,500 fbsl [158-316] mbsf); on the LWD logs, gas hydrate was identified in this interval in near-vertical fractures. The gamma ray in LWD Unit 2 is slightly lower than in the overlying section. Based on discontinuous and chaotic seismic reflections of variable amplitude, this section may be a mud-rich mass transport deposit (MTD). Near the bottom of Unit 2, a 2.5 m thick sand layer named the Red sand has the first high saturation hydrate in Hole H001 (Figure **F10**, top).

LWD Unit 3 underlies Unit 2 and extends from Hrz 0800 to Hrz 0500 (7,500-8,462 fbsl [316-610 mbsf]). In seismic data, LWD Unit 3 is characterized by continuous parallel reflections of moderate amplitude; the corresponding section in Hole H001 LWD has high gamma ray that changes to slightly lower gamma ray in the lower part of LWD Unit 3. LWD Unit 3 is interpreted as a hemipelagic mud-dominated section.

LWD Unit 4 extends from Hrz 0500 downward to Hrz 0400 (Blue) (8,462-8,747 fbsl [610-696 mbsf]). Hrz 0500 is a strong seismic reflector, that truncates underlying stratigraphy, marking an erosional surface (Figure **F5**, label erosion). Hrz 0500 is associated with abrupt increase in gamma ray with depth. The seismic reflection data within the lower-most section of LWD Unit 4, below Hrz 0500 is characterized by discontinuous reflections with variable amplitude. This section is interpreted as MTD, which may be silt-rich mud as indicated by moderately low gamma ray. Very thin low gamma-ray and low resistivity streaks within this zone indicate the presence of thin water-bearing coarse-grained intervals. The hydrate-bearing

https://doi.org/10.5281/zenodo.13971076

Upper Blue sand (Figure F10, middle) is near the base of this interval.

LWD Unit 5 starts at Hrz 0400 (Blue) (8,747 fbsl [696 mbsf]). The lower part of the Blue sand is not present at Hole H001. LWD Unit 5 contains Hrz 0300 (Orange), as indicated by low gamma ray values, and correlates to the top of the Orange sand. High resistivity, high P-wave velocity, and low density in the Orange sand indicates the presence of pore-filling, high saturation gas hydrate (Figure F10, bottom) (Frye et al., 2012, Collett et al., 2012); the hydrate saturation in the Orange sand is the highest of all the sands in Hole H001 (Figure F10, bottom).

Geothermal gradient and thermodynamic conditions

In-situ temperatures were estimated at Hole H001 (Figure F11). The estimated temperature was based on the following assumptions.

- At the depth of the interpolated bottom simulating reflector, methane is in three phase equilibrium (vapor-liquid-hydrate). The three-phase equilibrium for methane hydrates was derived using the model developed by Moridis et al. (2012).
- The pore fluid salinity is that of seawater (35 ppt).
- The pore pressure is hydrostatic and follows a gradient of 0.446 psi/ft (i.e., a fluid density equal to 1.03 g/cm^3).
- The seafloor temperature is 39.2 °F (4.0 °C) (Boyer et al., 2018).
- Temperature increases linearly with depth from the seafloor to the base of the hydrate stability zone.

The predicted in-situ temperature at Hole H001 is shown as a green dashed line in Figure F11. The BSR at Hole H001 is interpreted to be at ~9,397 fbsl. Based on this, at Hole H001, the temperature at the base of the hydrate stability zone is estimated to be 68.2 °F (20.1 °C) and the gradient to be 9.6 °F/1000 ft (17.5 °C/km). The LWD temperatures acquired

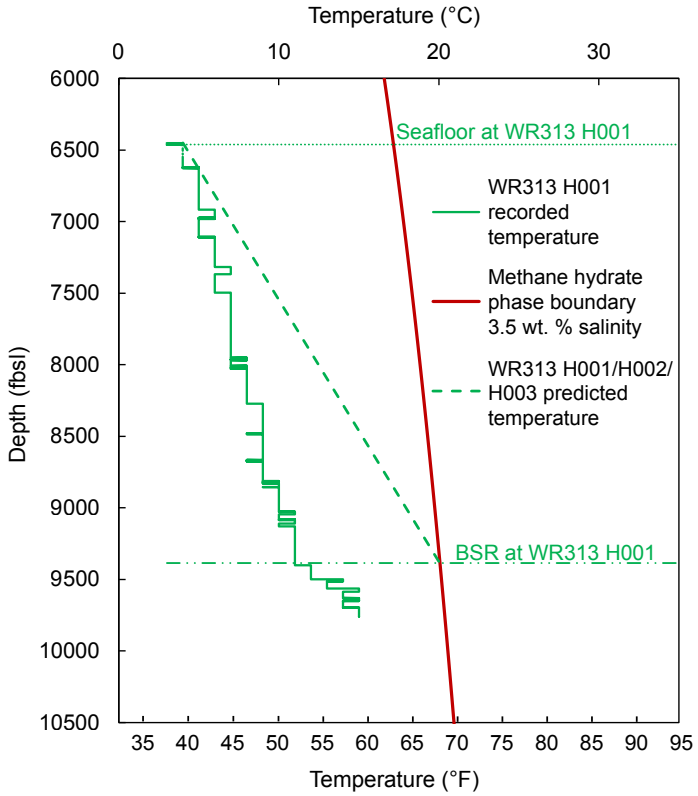

Figure F11: Estimated temperature profile from the seafloor to the bottom simulating reflector (BSR) at WR313 Hole H001 (green dashed line). Solid green line illustrates the logging while drilling (LWD) borehole temperature. The phase boundary for methane hydrate is delineated by the red line: hydrate is stable to the left of this line and not stable to the right. The horizontal green dash-dot line records the depth of the BSR. The system is assumed to be at the three-phase boundary at this depth as indicated by the crossing of the temperature profile with the methane hydrate stability boundary at the same depth.

during the drilling of Hole H001 (green solid line in Figure F11) illustrate that the borehole temperature during drilling is less than the formation temperature because colder fluids were being circulated downhole, which is commonly seen in marine scientific drilling (Collett et al., 2010).

Pore pressure and fracture gradient

There was no indication of abnormal pressure when Hole G001 was drilled (Collett et al., 2010). However, at Hole G001, at depths greater than 8,264 ft Rotary Kelly Bushing (RKB; see Methods: Depth units (Flemings et al., 2025b)), it was necessary to pump and rotate the drill string while simultaneously pulling out of the borehole, which was interpreted as

the borehole closing in on the bottom-hole assembly (BHA). At 9,244 ft RKB, a major blockage of flow occurred. Thereafter, the water-based mud weight was raised to 10 ppg and pumped continuously. At a depth of 9,599 ft RKB, the water-based mud weight was raised to 10.5 ppg. Thereafter, the well was drilled without incident (Collett et al., **2010**). The subsequent Hole H001 was drilled with 10.5 ppg below 8,501 ft RKB without incident.

Pre-drill pore pressure and fracture gradient profiles were constructed for Site H (Figure **F12**). The overburden stress (σ_v) was generated by integrating the density log from the LWD data in Hole H001. Pore pressures were assumed to be hydrostatic (u_h) because of the lack of evidence for elevated pore pressures while drilling Hole H001. The hydrostatic pore pressure (u_h) profile was expressed with a pore pressure gradient of 8.95 ppg (0.465 psi/ft). This hydrostatic gradient is slightly larger than the previously assumed 0.446 psi/ft. However, it reflects common practice in the drilling industry and was used in permitting the well. The least principal stress (σ_{hmin}) was estimated using Equation **E2**.

$$\sigma_{hmin} = K * (\sigma_v - u_h) + u_h$$

Equation E2.

Equation **E2** is commonly used to model the fracture gradient (Eaton, **1969**; Flemings, **2021**). An upper bound of $K = 0.9$ and a lower bound of $K = 0.7$ was assumed.

To avoid borehole closure at deeper depths when a weighted mud is not used as occurred for G001 (Collett et al., **2010**), the plan was to increase the drilling fluid weight at a depth of 8,113 ft RKB by switching to a 10.5 ppg water-based mud (gray horizontal line, Figure **F12**).

https://doi.org/10.5281/zenodo.13971076

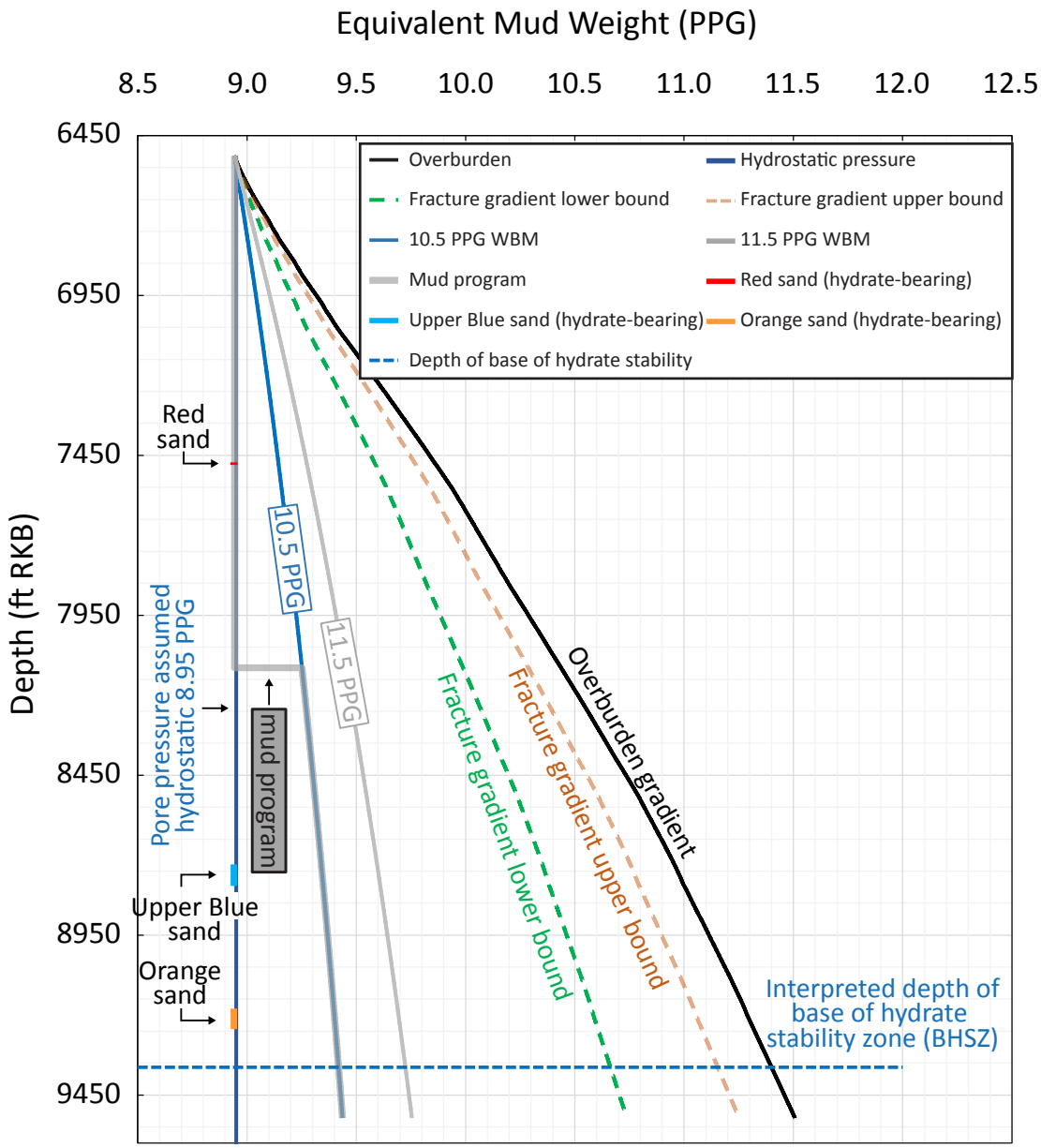

Figure F12: Pressure and fracture gradient plot for Site H in Walker Ridge Block 313 (WR313). The pore pressure is assumed to be hydrostatic (solid blue line). The overburden is shown with a solid black line. The fracture pressure is inferred to lie between the green and tan dashed lines based on assuming K = 0.7 and 0.9 in Equation **E2**. The planned mud program (gray solid line) shows the increase in mud weight to 10.5 ppg water-based mud (WBM) at 8,113 ft RKB.

Dan Minarich prepares the Geotek overpack system used to transport pressure cores over land to UT. Photo credit: Geotek Ltd.

Science objectives

The goals of this expedition were to better understand the potential of deepwater marine hydrate reservoirs to serve as an energy resource (see **Gas hydrates and energy**), and to illuminate the role of the marine hydrate system in the carbon cycle (see **Gas hydrates, the global carbon cycle, and the microbial factory**).

To accomplish these goals, we wished 1) to understand how coarse-grained hydrate reservoirs form and how carbon cycles through this sedimentary system where hydrate reservoirs reside, and 2) to understand the geological and petrophysical properties of the coarse-grained hydrate reservoir and its seals. These goals led to five principal objectives described below.

1. Characterize the Orange sand and Upper Blue sand hydrate reservoirs and their bounding units by determining:
   - hydrate saturation, dissolved methane concentration, and gas composition
   - pore water solute concentration and composition
   - sediment type (mineral and clay composition), grain size, and sorting
   - compressibility
   - strength behavior
   - sediment composition and age
   - microbial communities and activity
   - physical properties such as porosity, permeability, grain density, and liquid limit

https://doi.org/10.5281/zenodo.13971076

2. Obtain vertical high-resolution geochemical and sedimentary profiles by continuously coring to 500 fbsl and including:
    - pore water
    - sedimentology
    - physical properties
    - microbiological properties
    - mechanical properties
3. Measure the in-situ temperature and pressure profile
    - measure temperature with the Advance Piston Corer Temperature Tool (APCT-3)
    - measure both temperature and pressure with a Pore Pressure Penetrometer
4. Characterize the dissolved methane concentration and analyze the gas molecular and isotopic compositions with depth by collecting pressurized core samples and quantifying the gas content.
5. Describe occurrences of hydrate-bearing thin sands < 3m-thick and hydrate-bearing near-vertical fractures in marine muds which also occur at WR313.

Operational strategy to meet our objectives

The Operational Strategy is described in detail in the Operational Plan (Flemings et al., **2023b**) and Prospectus (Flemings et al., **2023a**).

The following operations were planned during the expedition to achieve our scientific objectives.

1. Pressure core analysis:
    - Obtain pressure cores from key hydrate-bearing sands, bounding muds, and background muds to meet Objectives 1, 4, and 5.
    - Conduct pressure core logging and imaging to determine the amount and quality of pressure core recovered, the amount of fall-in material, the lithofacies present, to discriminate hydrate-bearing sediment, and to determine core cutting locations.
    - Sample whole-round lithofacies-specific pressure cores for quantitative degassing and gas analysis, geomechanical testing, cryogenic freezing and depressurization for microbiology, rapid depressurization for pore water analyses, and distribution to other institutions.
        - Conduct quantitative degassing of hydrate bearing sands to measure dissolved methane concentration, hydrate saturation, and assess the composition and source of the dissociated gas.
        - Conduct quantitative degassing of clean background mud (no hydrate-filled fractures or coarse-grained beds/laminations) to measure the dissolved methane profile and gas composition with depth.
        - Collect and assess gas produced from quantitative degassing to determine hydrocarbon, carbon dioxide, and noble gas content and hydrocarbon isotope and isotopologue ratios.
        - Conduct cryogenic freezing and depressurization to preserve high-hydrate sections as intact cores for microbiological analysis.
        - Move all depressurized pressure core section that remain intact to the conventional core processing flow. Bag unconsolidated sediment from degassed core sections for mechanical studies (as a reconstituted core), physical properties, and biostratigraphy.
2. Conventional core analysis:
    - Obtain conventional cores to meet Objective 2
    - Conduct conventional core logging and measurements
        - Capture an immediate thermal imaging of the core to identify background sediments versus hydrate-bearing anomalies and provide an initial assessment of core quality.

    - Conduct core logging and imaging to inform stratigraphic context, track variation in sediment composition, and determine whole-round core sampling locations.
    - Measure sediment strength to characterize the mechanical state of the sediments as a function of depth and inform the switch from the Geotek-Advanced Piston Corer (G-APC) to the Geotek Extended Core Barrel (G-XCB) coring.
- Sample whole-round cores for void gas, headspace gas, pore water geochemistry, microbiology, physical properties, composition, cell counts, and geomechanics.
    - Conduct gas analysis to create a profile of hydrocarbon fluids and gases encountered at depth.
    - Conduct initial pore water analysis of ephemeral properties to determine the role of biogeochemical and alteration processes within sediments, as well as the contribution of advected deep fluids into the shallower hydrate stability zone.

3. Split core analysis:
    - Split intact core sections
    - Describe archival half visually
        - Document bedding, sedimentary structures, major lithology, relative grain sizes, Munsell color, presence of diagenetic nodules, bioturbation, and drilling/coring disturbance.
        - Conduct microscopic sediment analysis via smear slide and coarse fraction sampling and description to complete the lithostratigraphic core description and log.
        - Conduct coarse-fraction sediment analysis for identification of changes in bulk composition.
        - Conduct biostratigraphic observations of key nannofossil markers species to determining sediment age and sedimentation rates.
    - Conduct split cores logging and imaging to interpret depositional environments and geological history.
    - Sample working half to construct comprehensive core descriptions containing the compositional, structural, stratigraphic, and diagenetic fabric and facies variations throughout the cores.
4. Formation temperature measurements:
    - Measure formation temperature to meet Objective 3.

https://doi.org/10.5281/zenodo.13971076

University of Texas at Austin (UT) team members Alejandro Cardona, Donnie Brooks, and Josh O'Connell prepare the penetrometer for deployment. Photo credit: Geotek Ltd.

Site summary

Operational summary

A detailed review of Expedition UT-GOM2-2 Site H operations is provided in Expedition UT-GOM2-2 Site H (Flemings et al., **2025a**) and summarized below.

A graphical presentation of all operations at Site H is shown in Figure **F13**. Schedule and operational details for this expedition can be found in Site H: Operational summary (Flemings et al., **2025a**). Mobilization began on 30 July 2023 and continued for approximately 5 days. During mobilization, tools, personnel, equipment, supplies, and fluids were transferred to the Helix *Q4000* deepwater well intervention vessel (*Q4000*). Service vans were brought online, and downhole tools were tested.

UT-GOM2-2 was executed from 0000 hrs on 04 August 2023 to 2400 hrs on 30 August 2023 (27 days). Two "twinned" boreholes were drilled and cored adjacent to the original WR313-H001 (Hole H001) hole that was drilled during the 2009 Joint Industry Project Expedition II (Collett et al., **2012**) (Figure **F14**). See Site H: Surface location (Flemings et al., **2025a**). The calculated water depth at the start of each hole was 6,454 ft, 3 feet deeper than the measured depth at Hole H001. See Site H: water depth and rig floor elevation (Flemings et al., **2025a**).

Hole H003 was drilled first. Hole H003 is located 66 ft (20.12 m) NNE of Hole H001. Hole H003 was spudded with three successive G-APC hydraulic piston cores and continuously cored with both piston and pressure coring

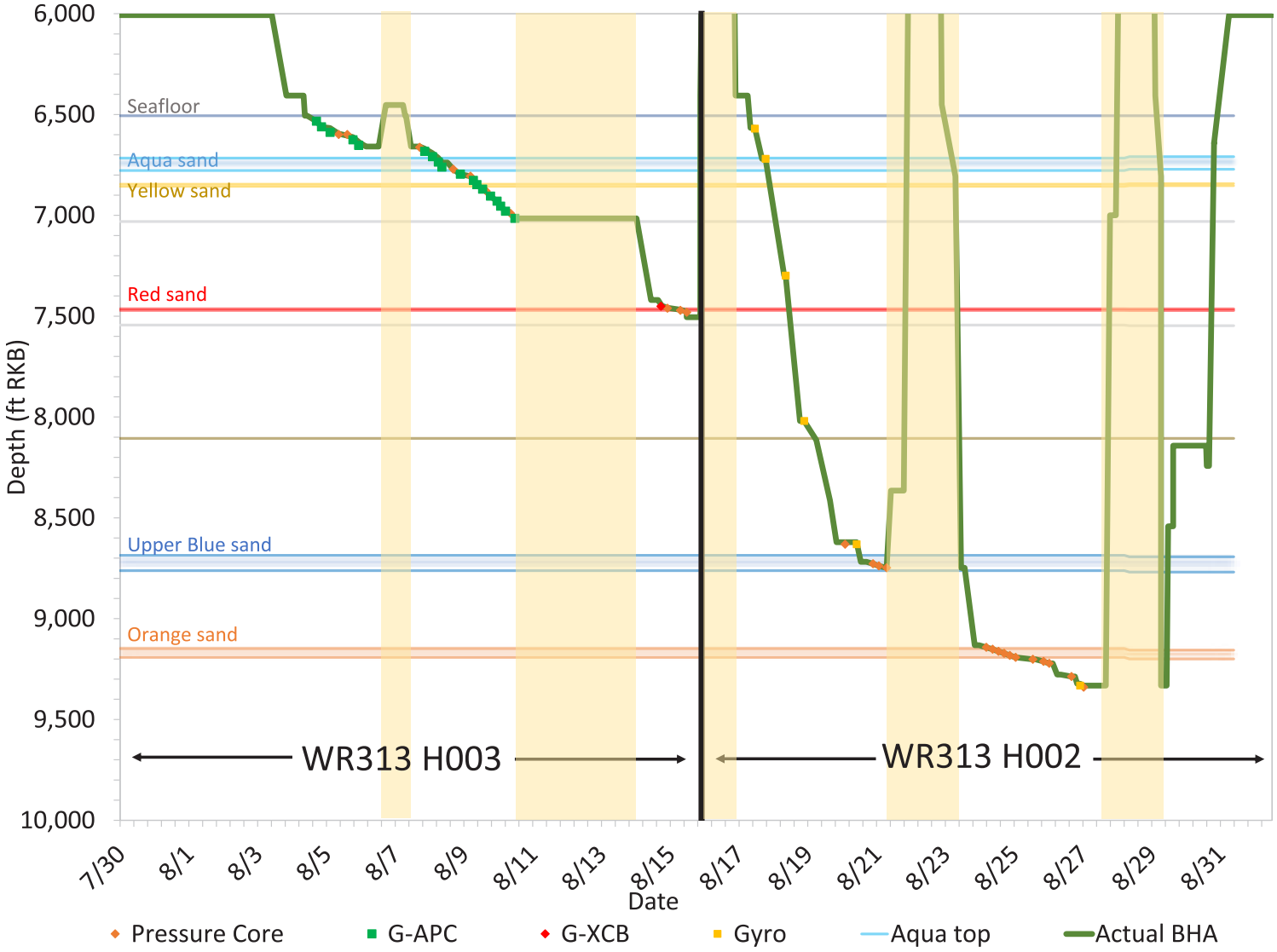

Figure F13: Measured depth of the bit depth as a function of time at Walker Ridge Block 313 (WR313) for Hole H002 and Hole H003. The measured depth of the bit is shown as a green line. On top of the green line, stops are shown for pressure coring as orange dots, conventional coring as green squares and red diamonds, and gyroscopic measurements as dark yellow squares. Operational downtime or non-productive time (NPT) is shown as transparent yellow columns. Projected sand depths are shown as aqua blue, yellow, red, blue, and orange horizontal lines. The projection of depths is discussion in Site H: Plotting H001, H002, and H003 downhole data (Flemings et al., **2025a**). A detailed review of Site H operations is provided in Site H: Operations (Flemings et al., **2025a**).

https://doi.org/10.5281/zenodo.13971076

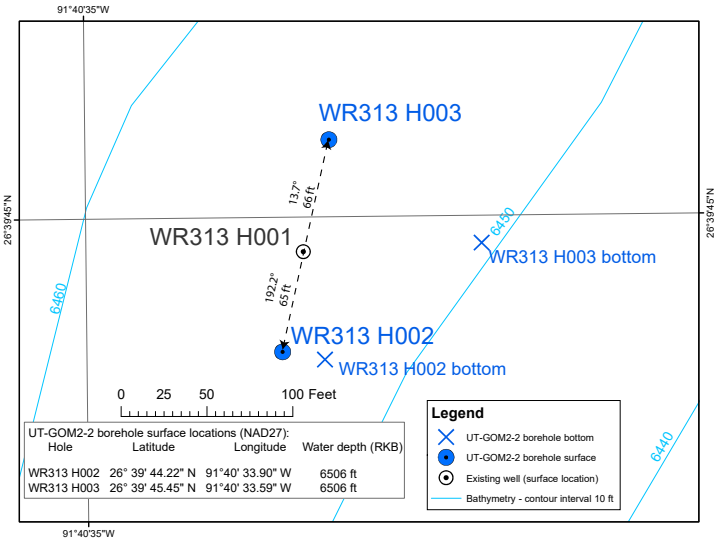

Figure F14: The locations, distances, and azimuths of the boreholes at Site H. Hole H001 location coordinates from the U.S. Bureau of Safety and Environmental Enforcement (BSEE, **2024**). The locations of Hole H002 and Hole H003 as surveyed by Fugro (top-hole) and Gyrodata (bottom-hole) during UT-GOM2-2. Bathymetry was derived from seafloor reflector in three-dimensional seismic data. WR313 = Walker Ridge Block 313; NAD27 = North America Datum of 1927. RKB = Rotary Kelly Bushing.

to 7,015 ft RKB (155.1 mbsf) with seawater. One G-XCB core and three pressure cores were acquired from 7,420 to 7,480 ft RKB (278.6 to 296.9 mbsf). See Coring. One deviation survey was conducted in Hole H003 after the borehole was advanced to a depth of 7,505 ft RKB. The borehole was found to trend ESE (Figure **F14**, WR313 H003 bottom) with inclination increasing from 6.06 degrees near the mudline to 7.75 degrees near the bottom of the borehole and the hole was abandoned. See Site H: Borehole deviation survey (Flemings et al., **2025a**). A projection of the stratigraphic depths in Hole H001 to Hole H003 was determined. This projection is applied to Hole H001 Depths when comparing Hole H001 LWD data to Hole H003 core data. See Site H: Projection of Hole H001 to Site H measured depth (Flemings et al., **2025a**).

Hole H002 was drilled second and is located 65 ft (19.8 m) SSW of Hole H001. Five directional surveys were conducted in Hole H002. They showed that the hole remained near vertical. See Site H: Borehole deviation survey (Flemings et al., **2025a**). Hole H002 was intermittently pressure cored from 8,620 ft RKB (644.3 mbsf) to a total measured depth of 9,332 ft RKB (861.3 mbsf) with 10.3 to 10.5 ppg water-based mud. Pressure coring included continuous coring of the Terrebonne Basin Orange sand and surrounding layers from 9,131 to 9,221 ft RKB (800.0 to 827.5 mbsf). See **Coring**.

During operations, non-productive time was incurred from tool pack-off, resulting in the BHA being partially or completely retrieved to the rig floor, *Q4000* Top Drive System (TDS) blower motor failure, and a piece of wireline lodged in the coring tool (Figure **F13**, yellow columns). Downhole tools became stuck inside the BHA three times because coarse-grained sediment packed off around the tool within the BHA. There are two possible root sources of this coarse-grained sediment. The first possibility is the sand layer present on the seafloor at Site H. This sand layer developed into a crater around the borehole and dumped sand into the borehole and made removal of the sand-sized particles and drill-cuttings more difficult. Several operational events described in Site H (Flemings et al., **2025a**) that also prevented circulation for significant periods, possibly exacerbated the problem. The other possible source of the coarse-grained sediment may have been associated with periods of non-circulation, which may have also caused barite to fall out of the water-based mud. See Site H: Drilling challenges (Flemings et al., **2025a**).

Demobilization from the site began on 31 August 2023. After completing the transfer of equipment and personnel, demobilization ended after 2 days, when the *Q4000* moved 1-mile off location on 01 September 2023. From the *Q4000*, conventional and conventionalized (depressurized pressure) cores were transported by Geotek to College Station, Texas for conventional core logging (MSCL-S and CT), and thirteen pressure cores were delivered to the UT Pressure Core Center. The remaining pressure core sections were transported to Geotek facilities in Salt Lake City, Utah for further processing. After logging, conventional and conventionalized cores were transported from College Station, Texas to Salt Lake City for further processing.

Equipment was remobilized in Salt Lake City. Core analysis and sampling was conducted from 19 September 2023 to 26 September 2023 (8 days).

Coring

Figure F15 illustrates the integrated coring program for Hole H002 and Hole H003. Hole H003 extended to 296.8 mbsf (Figure F15, column G). In Hole H003, eighteen G-APC, one G-XCB, and ten Pressure Coring Tool with Ball Valve (PCTB) cores were taken, with the PCTB cores being acquired using the Cutting Shoe configuration (PCTB-CS) (Figure F15, column I).

In Hole H003, continuous piston coring was performed to 7,015 ft RKB (155.1 mbsf) and thereafter intermittent cores were taken to a total depth of 7,480 ft RKB (296.8 mbsf) (Figure F15, column I). Twelve temperature measurements were made in conjunction with some of the piston cores (APCT-3, Figure F15, column H). Pressure cores were acquired at ~100 ft (31 m) intervals from the seafloor down to 6,990 ft RKB (147.6 mbsf) to measure the buildup of the dissolved methane concentration with depth (Figure F15, column I).

Hole H002 reached a total depth of 9,332 ft RKB (861.3 mbsf) (Figure F15, column G). Only pressure cores were taken in Hole H002, and these were focused in and around the Upper Blue and Orange hydrate-bearing sands (Figure F15, column I). Fifteen pressure cores were taken using two different configurations of the tool: the PCTB-CS and the Face Bit configuration (PCTB-FB) of the PCTB (Figure F15, column I).

Pressure core recovery and tool performance

Between the two boreholes, a total of 179.8 ft (54.8 m) of core was acquired from 25 deployments of the PCTB; there were 4 deployments of the Face Bit configuration (PCTB-FB), and 21 deployments of the Cutting Shoe configuration (PCTB-CS).

The PCTB-CS configuration enables the deployment of both conventional coring and pressure coring tools and was deployed in both boreholes. In contrast, the PCTB-FB has a unique bottom hole assembly (BHA) that does not allow the deployment of conventional coring tools and was only deployed in Hole H002. 105.0 ft (32.0 m) was retrieved at elevated pressure (green zones, Figure F15, column K) and the remaining 74.8 ft (22.8 m) was processed as conventional core (pink zones, Figure F15, column K). After pressure coring, most of the pressure core was quantitatively degassed and processed as conventional core. 29.3 ft (8.92 m) was kept at elevated pressure and transferred to UT Pressure Core Center for future testing.

During pressure coring, recovery was low in sand-prone sections. Figure F16 shows an example of the cores across the Red sand. In this case, 3 continuous pressure cores were taken (Core H003-27CS, H003-28CS, and H003-29CS). It is clear that in sands, where the LWD gamma ray values are low (Figure F16, column D), recovery is low (Figure F16, column J, Core H003-28CS). In contrast, where the section is more mud prone, recovery is much higher (Figure F16, column J, Core H002-27CS, and -29CS). This behavior was again observed during pressure coring of the Upper Blue and Orange sands.

There were 25 pressure core deployments and one pressure coring test. Sixteen pressure cores (64%) were recovered at elevated pressure (Figure F15, column J, green boxes). Nine (36%) were recovered at atmospheric pressure (Figure F15, column J, pink boxes) when the PCTB failed to seal. Several failures were due to fall-in sediment jamming the ball and debris in the tool. Most cores that sealed did not seal at coring depth, but instead sealed as the core barrel was being raised in the pipe. See Site H: Pressure coring for more details (Flemings et al., 2025a).

Conventional core recovery and tool performance

From both boreholes, 533 ft (162.6 m) of conventional core was acquired. Cores were mostly expansive, and conventional coring generally had recoveries greater than 100% (Figure F15, column J). Core expansion resulted in an average recovery of sediment compared to the coring interval of 122%.

https://doi.org/10.5281/zenodo.13971076

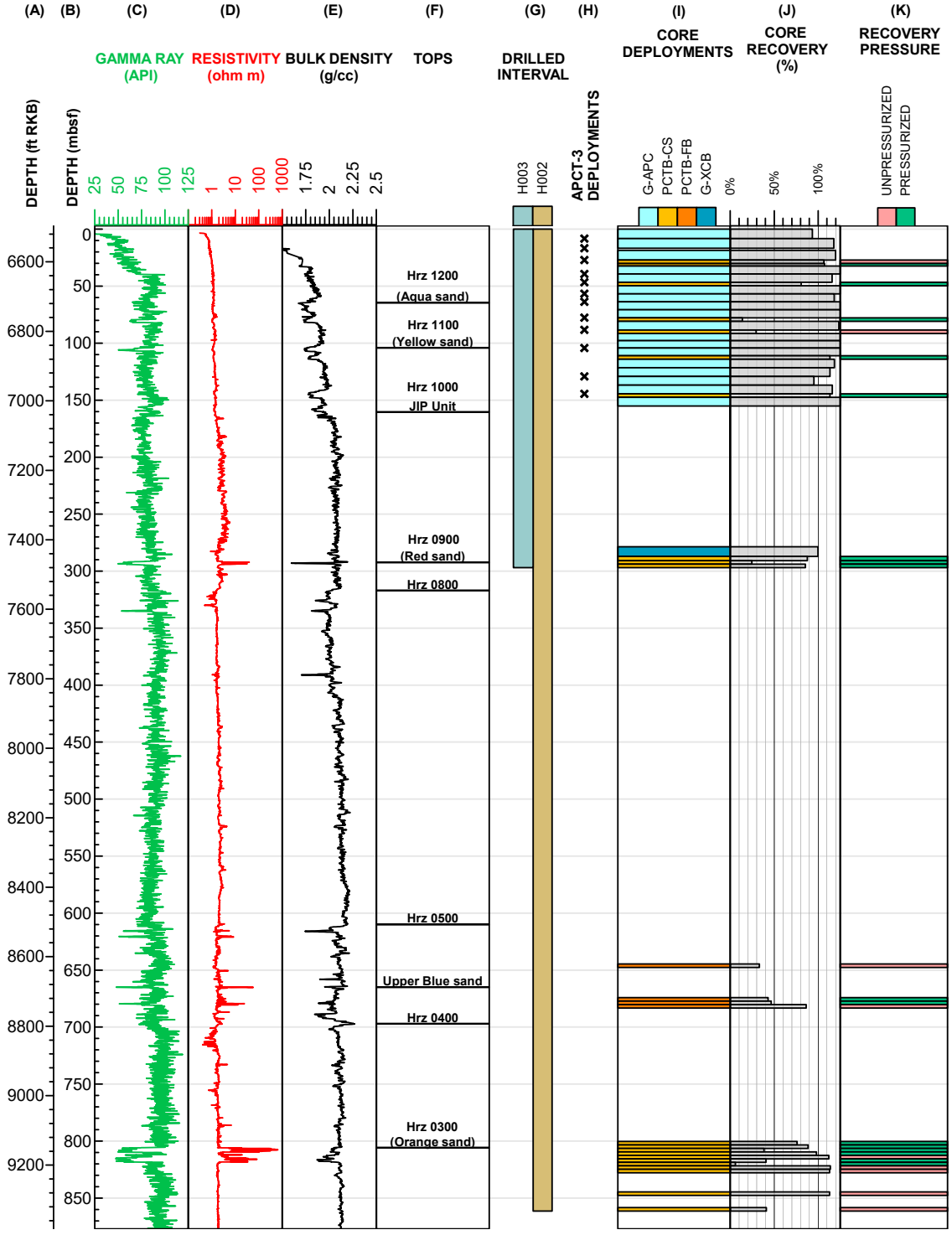

Figure F15: Core deployments and temperature measurements made during UT-GOM2-2. A) Measured depth in feet below rig floor (ft RKB); B) Measured depth in meters below the seafloor (mbsf); C) Projected logging while drilling (LWD) gamma ray in green. The depth projection of Hole H001 LWD data onto Hole H002 and Hole H003, used in columns C, D, E, and F, is discussed in Site H (Flemings et al., 2025a); D) Projected LWD resistivity in red; E) Projected LWD bulk density in black; F) Seismic horizons (Hrz) and stratigraphic tops as described in Site H: Plotting H001, H002, and H003 downhole data (Flemings et al., 2025a); G) Drilled interval for Hole H003 in blue and Hole H002 in tan; H) In-situ temperature measurement locations made with the Advanced Piston Coring Temperature Tool (APCT-3); I) Core deployments. Advanced Piston Cores (G-APC) are shown in light aqua blue. Extended Core Barrel (G-XCB) cores are shown in dark aqua blue. Core acquired using the Pressure Coring Tool with Ball Valve (PCTB) in the Cutting Shoe configuration (PCTB-CS) are shown in dark yellow and in the Face Bit configuration (PCTB-FB) in orange; J) Percent core recovery; K) Recovery pressure for the pressure cores measured with a pressure gauge on the rig. Cores recovered at elevated pressure are shown as green, and atmospheric pressure are shown as pink. A discussion about pressure coring operations and sealing is presented in Site H: Pressure coring (Flemings et al., 2025a).

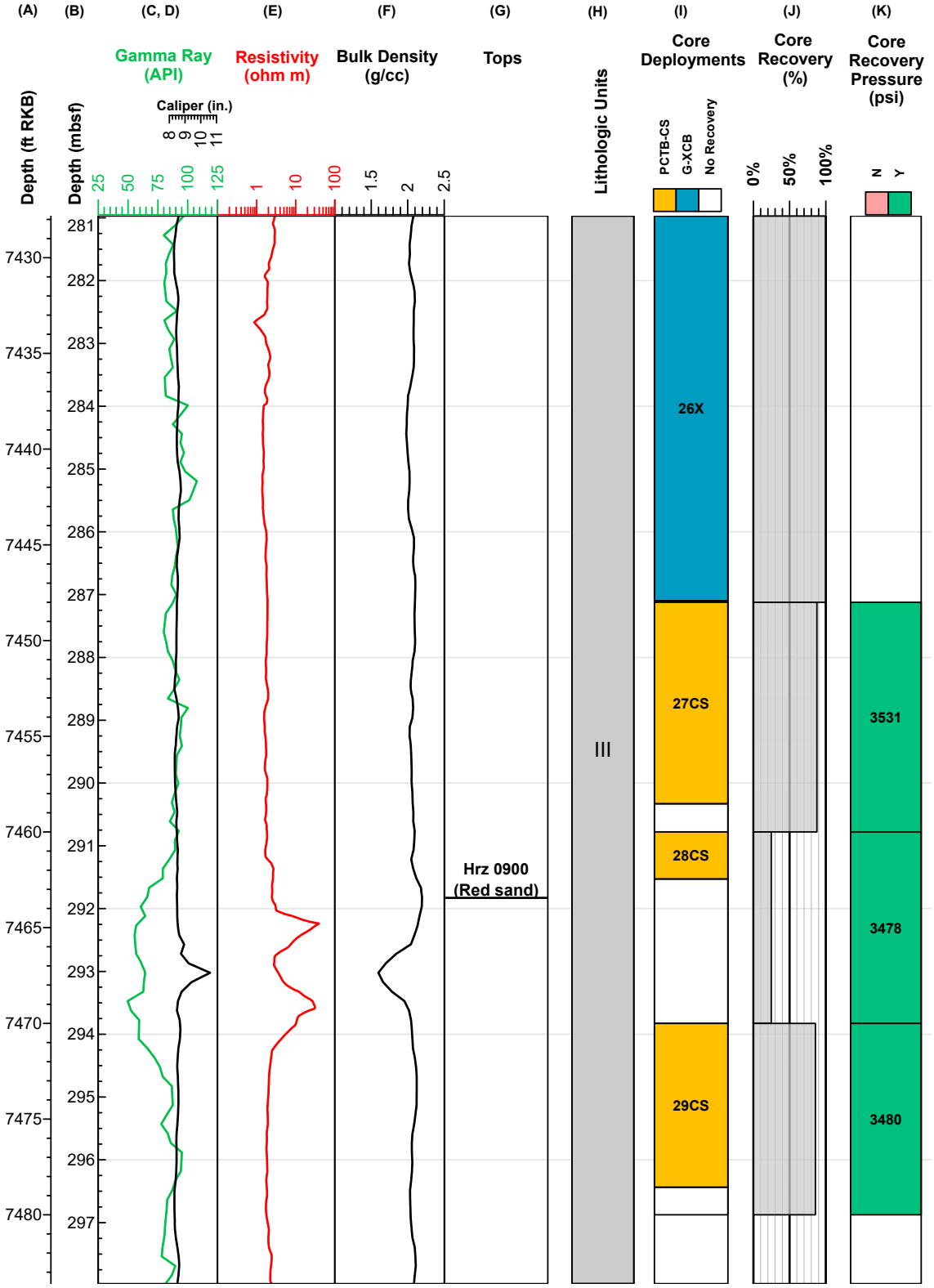

Figure F16: Core deployments at the Red sand. A) Measured depth in feet below rig floor (ft RKB); B) Measured depth in meters below the seafloor (mbsf); C) Projected logging while drilling (LWD) gamma in green. The depth projection of Hole H001 LWD data onto Hole H002 and Hole H003, used in columns C, D, E, F, and G, is discussed in Site H (Flemings et al., 2025a); D) Projected LWD caliper in black; E) Projected LWD resistivity in red; F) Projected LWD bulk density in black; G) Seismic horizons (Hrz) and stratigraphic tops as described in Site H (Flemings et al., 2025a); H) Lithologic units; I) Core deployments. Extended Core Barrel (G-XCB) cores are shown in dark aqua blue. Pressure Coring Tool with Ball Valve in the Cutting Shoe configuration (PCTB-CS) are shown in dark yellow. Area cored but not recovery is shown with gray diagonal hatches; J) Percent core recover; K) Recovery pressure for the pressure cores measured with a pressure gauge on the rig. Cores recovered at elevated pressure are shown as green. A discussion about pressure coring operations and sealing is presented in Site H: Pressure coring (Flemings et al., 2025a).

https://doi.org/10.5281/zenodo.13971076

G-APC cores were planned at less than the 31 ft (9.5 m) core liner length to account for expansion. This was accomplished by firing the G-APC a short distance above the top of the formation. G-APC deployments achieved full penetration through Core H003-21H (6930 ft RKB [129.2 mbsf]). G-APC refusal occurred with the acquisition of Core H003-25H when full stroke of the tool was not achieved. G-XCB coring was used to acquire Core H003-26X (7420 ft RKB [278.6 mbsf]).

Samples of sediments taken from a variety of cores prepared for “headspace gas” sampling. Credit: Jackson School of Geosciences

Initial results

In this section we summarize results from four types of studies: 1) Lithostratigraphy, 2) Calcareous nannofossil biostratigraphy, 3) In-situ temperature, and 4) Methane concentrations, hydrate saturation, and gas geochemistry. These examples highlight and integrate results across the drilling program. The results described here are presented in much more detail in Flemings et al. (**2025a**). In addition, other significant results not described here are also presented in Flemings et al. (**2025a**).

Lithostratigraphy

We integrated core data from Hole H002 and Hole H003 and LWD data from Hole H001 to describe seven successive lithologic units that are composed of one or several lithofacies (Figure **F17**, column H and I). A detailed discussion of how these lithologic units were defined and what lithofacies are present within these lithologic units are described in Site H: Lithostratigraphy (Flemings et al., **2025a**). We review these lithologic units below:

Lithologic Unit I (0-4.5 mbsf)

Unit I is a massive silt- to very fine sand encountered from the seafloor to a depth of 4.5 meters (Figure **F18**). The Massive Sand lithofacies was not interpreted prior to drilling. During drilling, this sand repeatedly slid into the

 https://doi.org/10.5281/zenodo.13971076

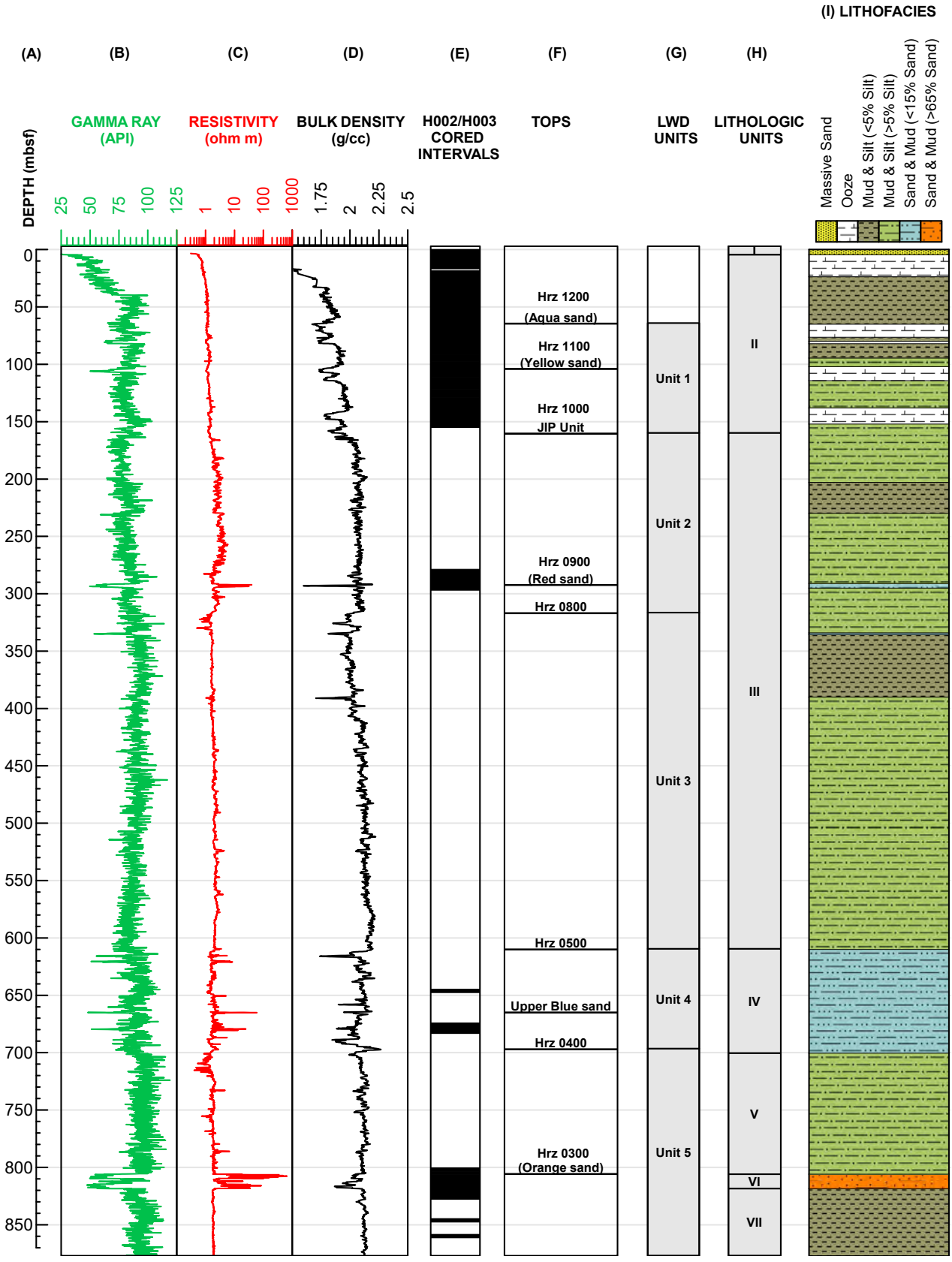

Figure F17: Interpreted Site H lithologic units and lithofacies. A) Measured depth in meters below the seafloor (mbsf); B) Projected logging while drilling (LWD) gamma ray in green; C) LWD resistivity in red. The depth projection of Hole H001 LWD data onto Hole H002 and Hole H003, used in columns B, C, D, F, and G, is discussed in Site H (Flemings et al., 2025a); D) Projected LWD bulk density in black; E) Cored interval for Hole H003 and Hole H002 in black; F) Seismic reflectors (Hrz = Horizon) and stratigraphic tops as described in Site H: Plotting H001, H002, and H003 downhole data (Flemings et al., 2025a); G) LWD units (See **Site H seismic and LWD interpretation**); H) Lithologic units; I) Lithofacies.

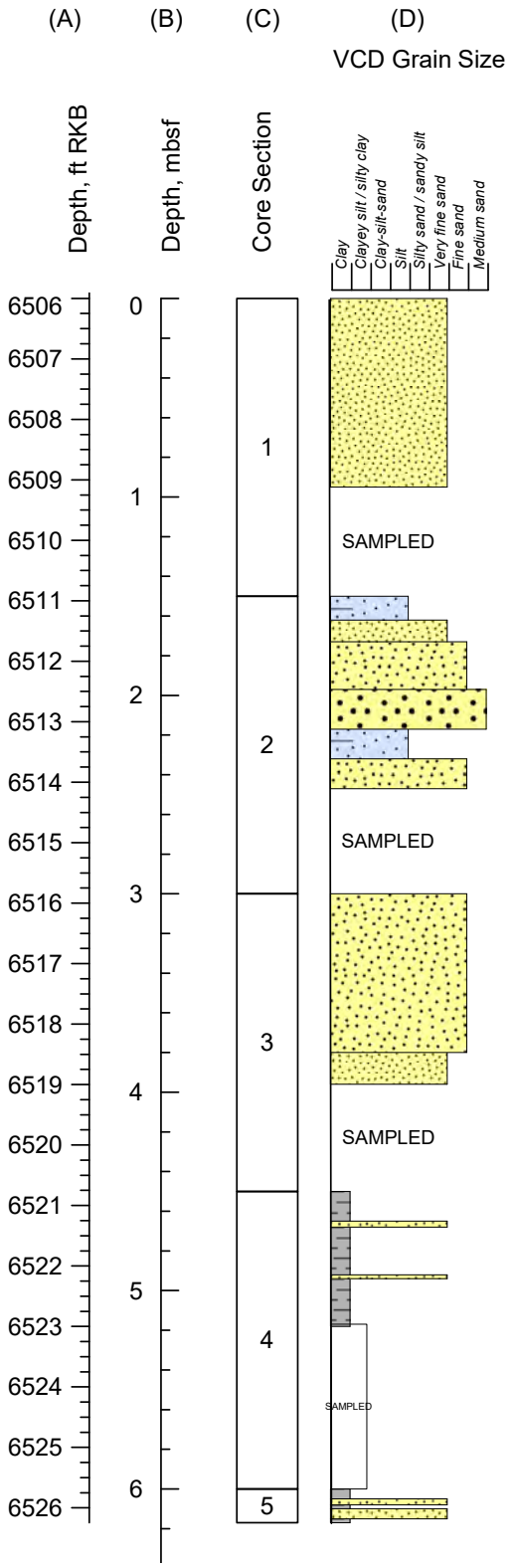

Figure F18: Visual core description (VCD) of the grain size at the top of Site H. Core H003-01H was taken at the seafloor and was the first core taken during drilling. A) Measured depth in feet below rig floor in feet (ft RKB), B) Measured depth in meters below seafloor (mbsf), C) Core Section number, D) VCD of grain size. Yellow is sand. Blue is silt. Gray is clay. See Methods: Grain size (Flemings et al., 2025b); Further discussion of this sand is provided in Site H: Drilling challenges and lithostratigraphy (Flemings et al., 2025a).

borehole, which may have contributed to packing off of the bottom hole assembly at deeper depths (see Site H Drilling Challenges (Flemings et al., 2025a). Kumar et al. (2024) suggest that this sand either reflects expulsion of sand from the deeper sands penetrated at Hole H001 during JIP II (Collett et al., 2012) or it represents a recent slope failure from the nearby uplifted salt ridge.

Lithologic Unit II (4.5-160 mbsf)

Unit II is composed of interbedded Ooze with Mud & Silt (Figure F19, column C). The LWD density log from H001 is expressed as a porosity (Figure F19, column E, blue line): the ooze has a higher porosity than the intervening muds. Direct measurements of porosity confirm that the ooze has significantly higher porosity than the mud intervals (Figure F19, column E, orange triangles and black circles). The ooze has a relatively high percentage of calcareous nannofossils (Figure F19, column D), and low magnetic susceptibility (Figure F19, column F).

Lithologic Units III (160-610 mbsf), V, and VII

Units III, V, and VII (Figure F17, column H) have high LWD Gamma Ray values (Figure F17, column B) and are composed of the Mud & Silt lithofacies (Figure F17, column I). Mud dominates with occasional millimeter to centimeter scale silt/sand layers (Figure F20, column B). The mud is a silty clay grain size when analyzed with the hydrometer method (Figure F20, column C).

Lithologic Units IV (Blue sand) and VI (Orange sand)

Unit IV (Upper Blue sand) and VI (Orange sand) are composed of interbedded sand and mud, termed the Sand & Mud lithofacies. These horizons are recognized as significant hydrate reservoirs in the Terrebonne basin and were key targets of Expedition UT-GOM2-2 (Frye et al., 2012; Meazell and Flemings, 2022) (Figures F17, F6, and F7). In Hole H002, Unit IV (Upper Blue sand) has a smaller fraction of sand (<15%) relative to Unit VI (Orange sand) (>15%). The

https://doi.org/10.5281/zenodo.13971076

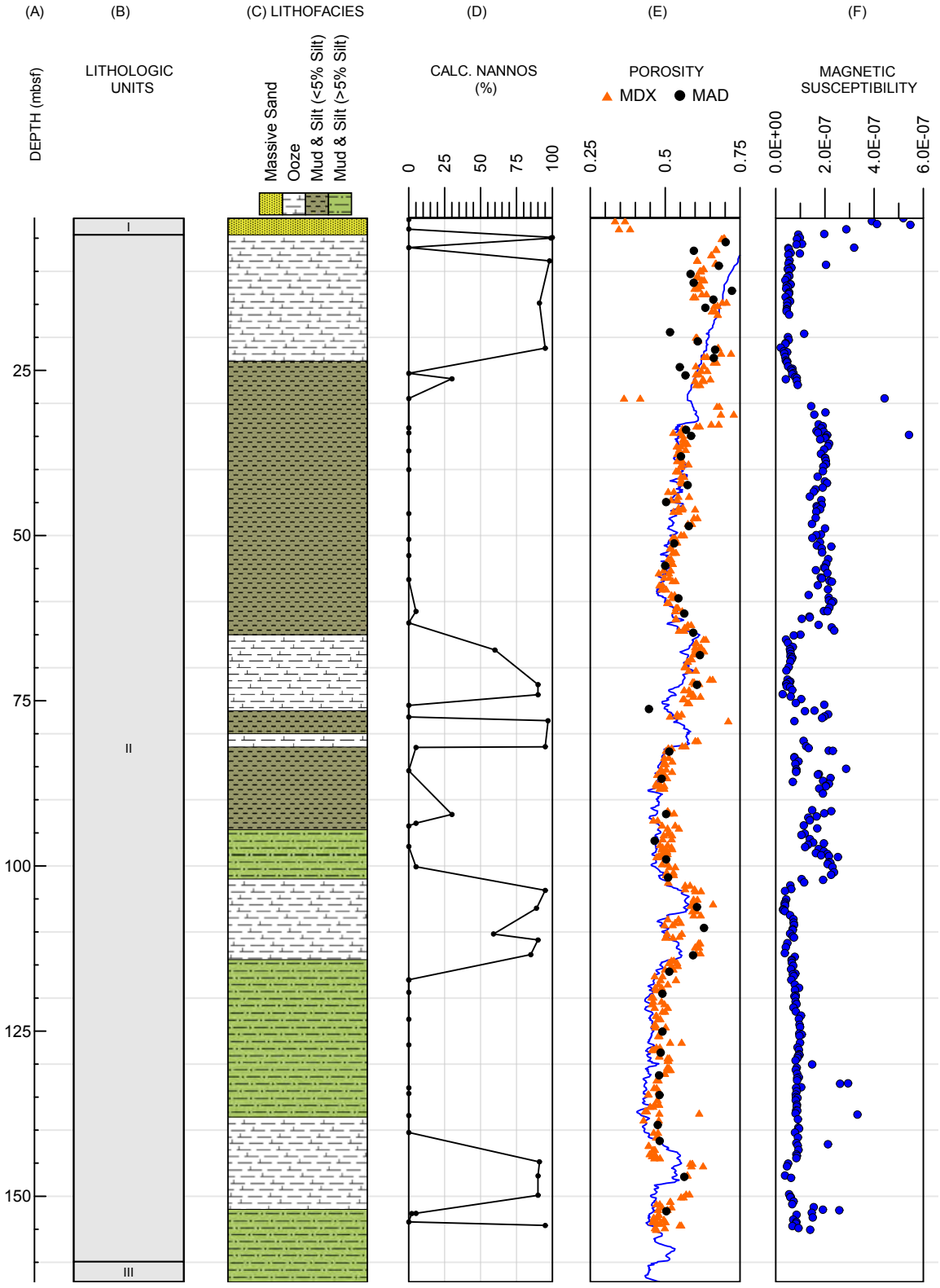

Figure F19: Lithologic Unit II. A) Measured depth in meters below the seafloor (mbsf); B) Lithologic units; C) Lithofacies; D) Fraction of calcareous nannofossils based on smear slide analysis in compressed measured depth; E) Porosity in compressed measured depth. Data from discrete split core plugs (sample code MDX) are shown as orange triangles. Data from discrete plugs taken from moisture and density whole-round samples (sample code MAD) are shown as black circles. Any measurements of samples containing fall-in or thin interbedded sand were not removed. Core porosity was determined assuming a fresh-water saturation of 100% and a grain density of 2.7 g/cm^3. Projected Hole H001 Logging while drilling (LWD) data are shown as a blue line. The depth projection of Hole H001 LWD data onto Hole H002 and Hole H003, used in columns B, C, D, F, and G, is discussed in Site H (Flemings et al., **2025a**); F) Magnetic susceptibility. Methods and further discussion of the biostratigraphy, index properties, and magnetic susceptibility can be found in the associated sections of Methods (Flemings et al., **2025b**) and Site H (Flemings et al., **2025a**).

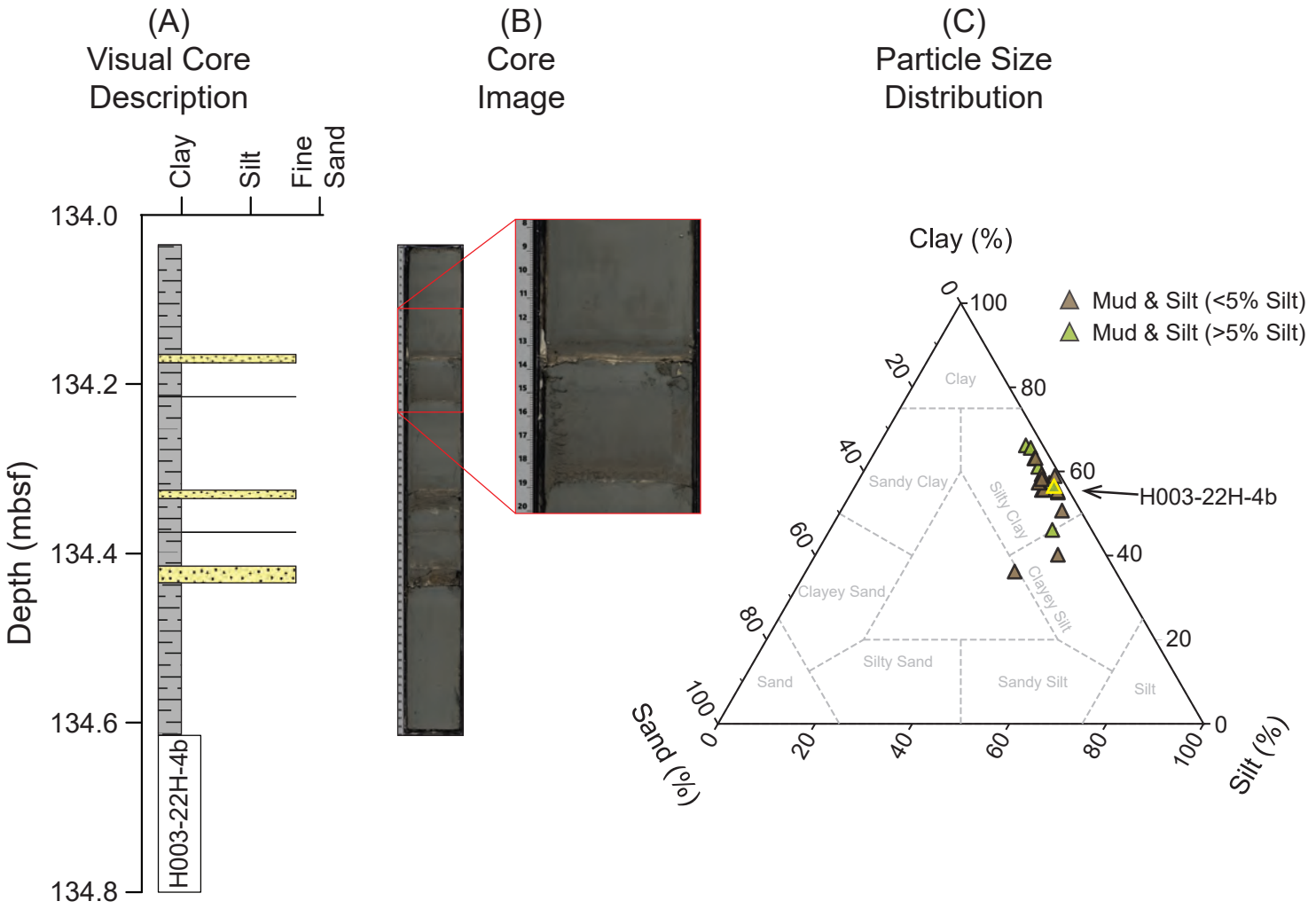

Figure F20: Illustration of Lithologic Units III, V, and VII. A) Visual core description of Section H003-22H-4 including location of moisture and density whole-round sample H003-22H-4b. Measured depth in meters below the seafloor (mbsf); B) Split Core image of Section H003-22H-4a after the sample was removed. The expanded view shows two silt layers; C) Ternary plot of particle size distribution of Mud & Silt lithofacies samples. Particle sizes were determined using the hydrometer method and classified using the geotechnical classification (particle size cutoffs of clay = <2 µm, silt = 2-75 µm, sand = >75 µm). The yellow highlighted triangle is sample H003-22H-4b. Methods and further discussion of the visual core description, core imaging, and particle size distribution can be found in the associated sections of Methods (Flemings et al., 2025b) and Site H (Flemings et al., 2025a).

lower sand/silt percentage of Unit IV relative to Unit VI is illustrated by the weaker gamma ray response in Unit IV relative to Unit VI (Figure F17, column B).

Figure F21 spans Unit VI, the Orange sand. Low LWD GR values (Figure F21, column B) are generally associate with high resistivity (Figure F21, column D) and high velocity (Figure F21, column E). Prior to our coring program, these zones were interpreted to record hydrate bearing horizons. The PCATS density (Figure F21, column F) and velocity (Figure F21, column G) data show that these zones have intervals of low density and high core velocity.

The sand/silt beds range in thickness from millimeter to decimeter scale as seen in Core H002-09CS (Figure F22, columns E and F). Occasionally graded bedding can be observed in the sand/silt intervals (Figure F22, column C). Most of the intervals contain more silt than sand when measured by laser particle analysis, except for one 40 cm interval near the top of Core H002-09CS (Figure F22, column D). The net to gross ratio of silt to sand layer thicknesses is greater than 50% (Figure F22, column F).

Figure F23 provides an expanded view of the hydrate-bearing sand interval in Unit VI (Orange sand) Core H002-07CS. The lower half of the recovered interval

https://doi.org/10.5281/zenodo.13971076

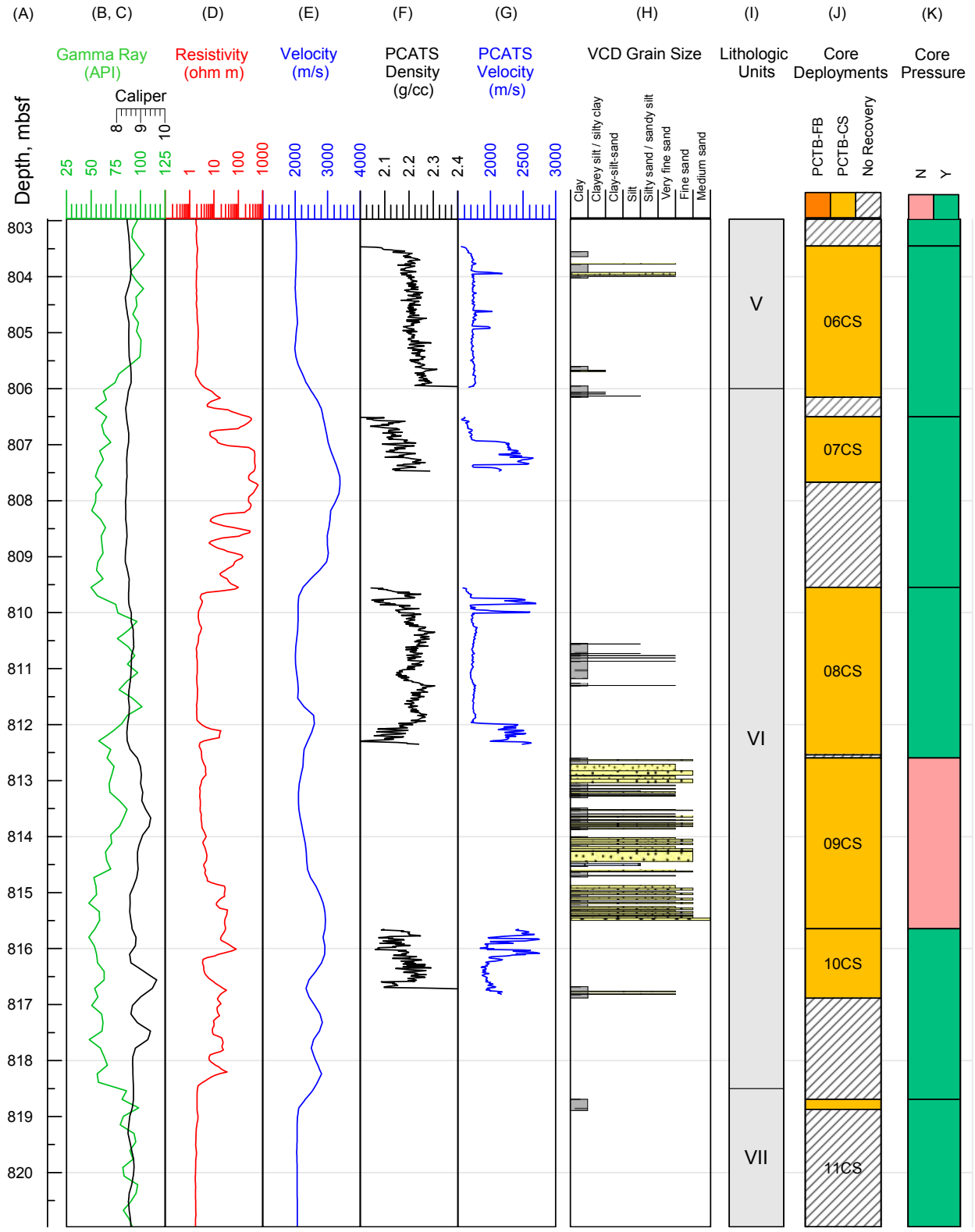

Figure F21: Lithologic Units V, VI and VII. Lithologic Unit VI is composed of the Mud & Sand lithofacies and is also called the Orange sand. A) Measured depth in meters below the seafloor (mbsf); B) Projected logging while drilling (LWD) gamma ray in green. The depth projection of Hole H001 LWD data onto Hole H002 and Hole H003, used in columns, B, C, D, and E, is discussed in Site H (Flemings et al., 2025a); C) Projected LWD caliper in black; D) Projected LWD resistivity in red; E) Projected LWD velocity in blue; F) Pressure Core Analysis and Transfer System (PCATS) gamma density in black; G) PCATS pressure core P-wave velocity in blue; H) Visual core description (VCD) of grain size: sands = yellow, silts = blue, clay = gray. I) Lithologic units, J) Core deployments using the Pressure Coring Tool with ball valve in the Cutting Shoe configuration (PCTB-CS) shown in dark yellow; K) Recovery pressure for the pressure cores measured with a pressure gauge on the rig. Cores recovered at elevated pressure are shown as green, and atmospheric pressure are shown as pink. An expanded view of Lithologic Unit VI Core H002-09CS is presented in Figure F22 and H002-07CS in Figure F23.

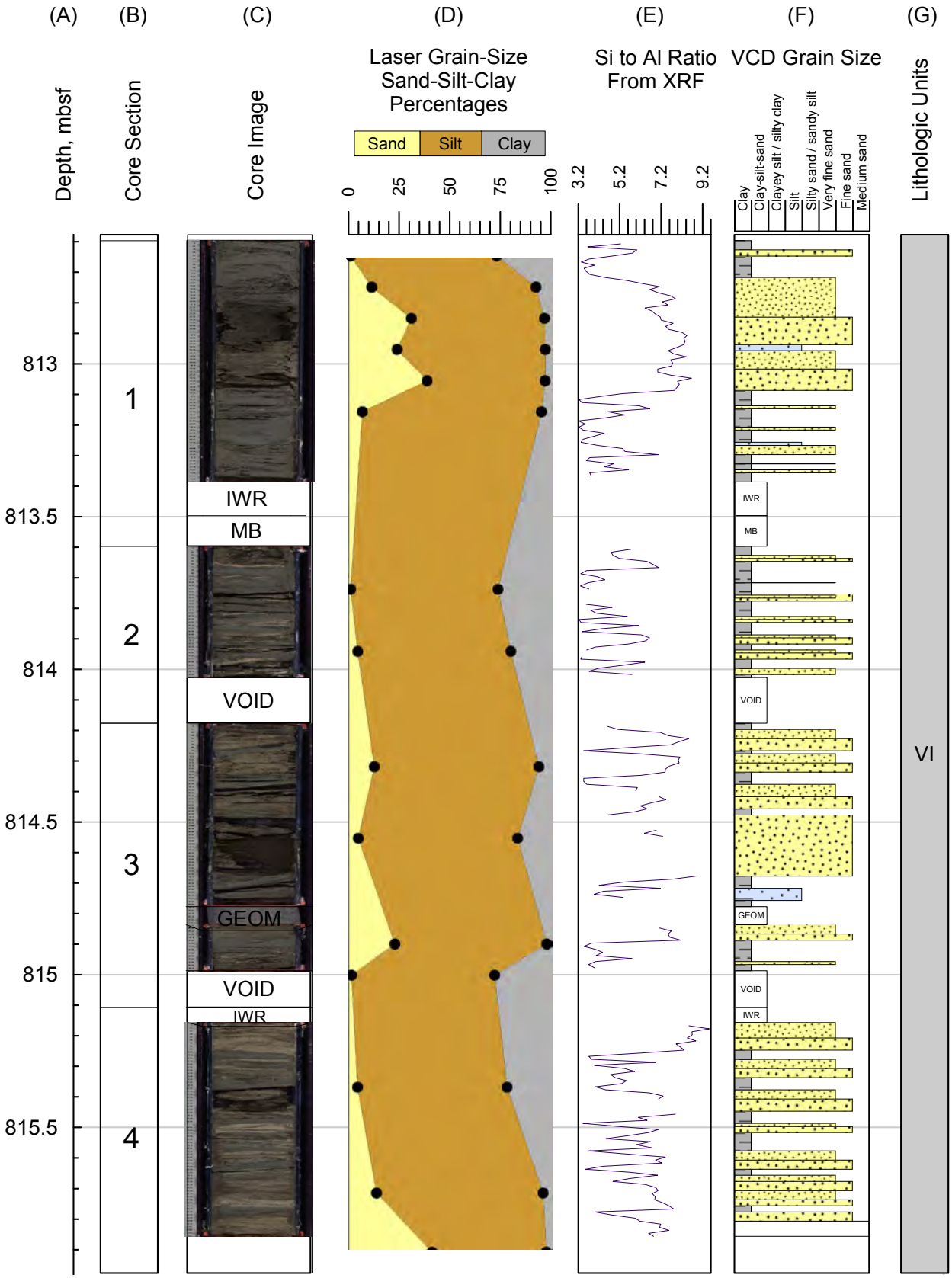

Figure F22: Expanded view of Lithologic Unit VI Orange sand (Core H002-09CS). This core was recovered at atmospheric pressure and thus was split, sampled, and described. A) Measured depth in meters below seafloor (mbsf); B) Section number; C) Split core images from the line scanner; D) Particle size distribution from laser particle analysis using the geoscience classification; E) Uncalibrated silicon to aluminum ratio calculated from X-ray fluorescence (XRF); F) Visual core description (VCD) of grain size: sands = yellow, silts = blue, clay = gray. Methods and further discussion of the visual core description, core imaging, and particle size distribution can be found in the associated sections of Methods (Flemings et al., 2025b) and Site H (Flemings et al., 2025a).

https://doi.org/10.5281/zenodo.13971076

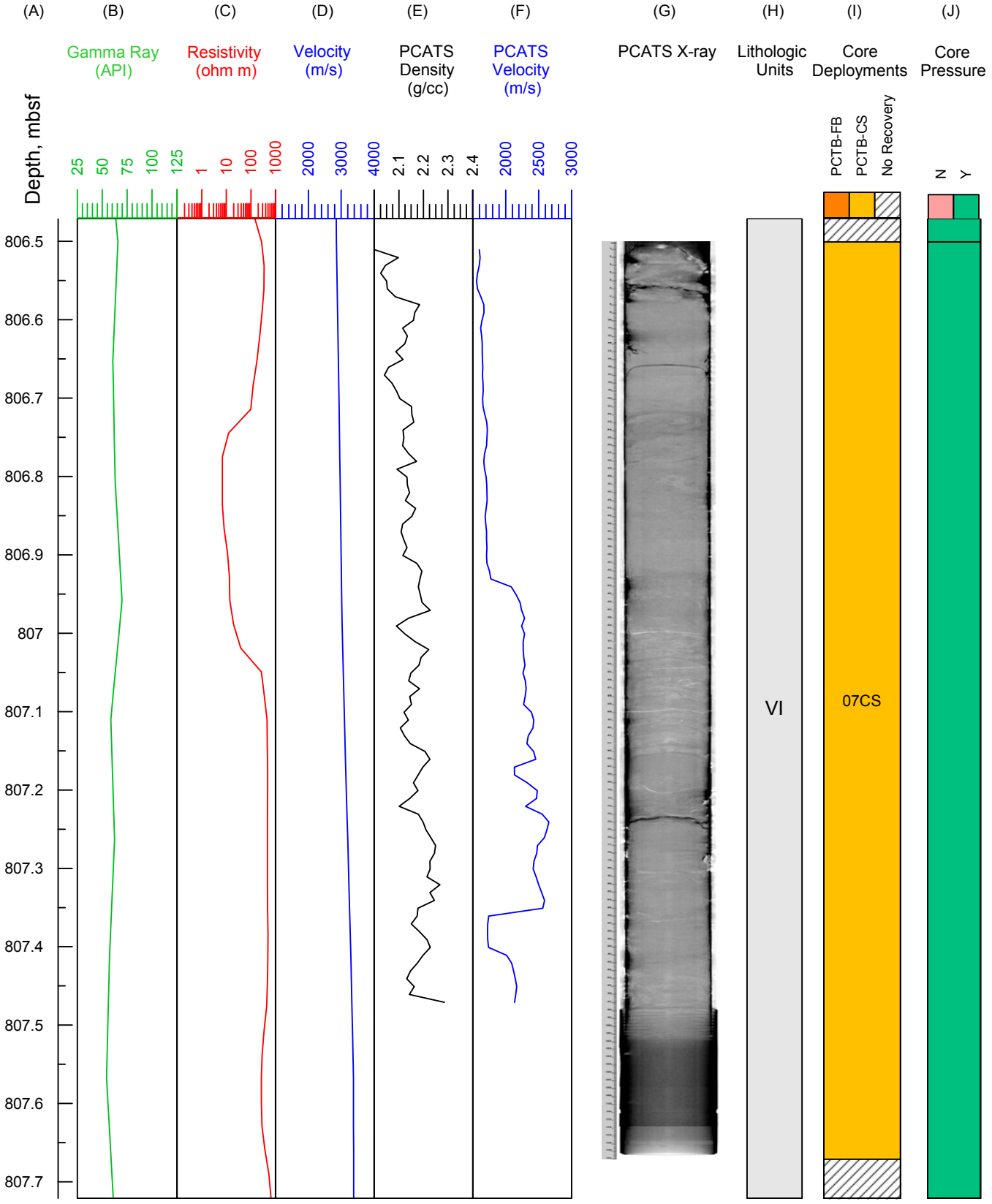

Figure F23: Expanded view of Lithologic Unit VI Orange sand (Core H002-07CS). A) Measured depth in meters below seafloor (mbsf); B) Projected logging while drilling (LWD) gamma ray in green. The depth projection of Hole H001 LWD data onto Hole H002 and Hole H003 is discussed in Site H (Flemings et al., 2025a); C) Projected LWD resistivity in red; D) Projected LWD Velocity in blue; E) Pressure Core Analysis and Transfer System (PCATS) gamma density in black; F) PCATS pressure core P-wave velocity in blue; G) PCATS X-ray; H) Lithologic units; I) Core deployments; J) Recovery pressure for the pressure cores measured with a pressure gauge on the rig. Cores recovered at elevated pressure are shown as green. Methods and further discussion of core logging and imaging, and pressure coring can be found in the associated sections of Methods (Flemings et al., 2025b) and Site H (Flemings et al., 2025a).

has high velocity and is interpreted to be a sand rich interval with a high concentration of hydrate.

Calcareous nannofossil biostratigraphy

340 samples were examined for calcareous nannofossil assemblages. Six Pleistocene calcareous nannofossil biohorizons were encountered over the combined depth of Hole H003 and H002 (Figure F24). The youngest biohorizon (the cross-over in dominance from *Gephyrocapsa* spp. to *E. huxley*i) was encountered at approximately 17 mbsf and is 0.085 Ma. The oldest biohorizon encountered was *P. lacunosa* C at 0.83 Ma (Figure F24). All strata penetrated are estimated to be a Pleistocene age (<0.91 Ma). A detailed discussion of the nannofossil biostratigraphy is given in Flemings et al. (2025a).

There is a striking decrease in accumulation rate with time. Lithologic Units III-VI lie within the zone of rapid accumulation and record an accumulation rate that decreases from 4.4 to 3.4 mm/yr. Unit II is deposited much more slowly with accumulation rates decreasing from 0.39 to 0.86 mm/yr upward through the section.

In-situ temperature

Discrete measurements of in-situ temperature at multiple depths in Hole H003 were made with the APCT-3. This is an instrumented cutting shoe that measures temperature while piston coring. See Methods (Flemings et al., 2025b).

The inferred in-situ temperature profile with depth for Hole H003 is shown in Figure F25. The temperature gradient from these measurements is inferred to be 25 °C/km. However, the estimated temperature gradient based on the depth of the BSR is estimated to be 17.5 °C/km (Figure F25, solid black line). The gradient of 17.5 °C/km is an average value across the entire hydrate stability zone down to the BSR at about 895 mbsf. By contrast, this measurement-based temperature gradient of 25 °C/km is for the first 150 mbsf. This discrepancy remains a challenge for future analysis.

Methane concentrations, hydrate saturation, and gas geochemistry

The concentration of methane present or the methane hydrate saturation was calculated based on the volume of the sample, a calculated porosity, a typical hydrate stoichiometry, and a typical hydrate density (Dickens et al., 2000). If the total amount of methane present was less than the in-situ maximum solubility of methane in water, then the sample did not contain methane hydrate, and the dissolved methane concentration was calculated. If the total amount of methane was greater than the in-situ maximum solubility of methane in water, the consequent hydrate saturation of the pore space was calculated based on the amount of methane in excess of the solubility limit.

We conducted quantitative measurements of the volume of gas and liquid produced during the stepwise depressurization of pressure cores to atmospheric pressure on 22 pressure core sections. Most of these analyses were performed on mud-rich material. One sample contained a transition from clay to sand rich layers of Lithologic Unit IV (Blue sand) at 675.13-675.33 mbsf (Section H002-2FB-4). The volume of gas produced was used to determine the in-situ concentration of dissolved methane in the pore water, the presence of methane hydrate, and the saturation of the pore space with methane hydrate.

Figure F26 illustrates the total volume of gas produced for three samples, one where no hydrate was present (Figure F26, Section H003-24CS-2, brown circles) and two where the dissolved methane concentration of the pore water was saturated and the core contained methane hydrate (Figure F26, Section H003-29CS-3 orange diamonds and Section H002-02FB-4 blue triangles).

During depressurization of the sample without hydrate (Section H003-24CS-3) only 1.66 L of methane was produced from a 94 cm long section of pressure core. When methane hydrate is present in low concentration (H003-29CS-3, Figure F26 orange diamonds), there is an abrupt bend present at ~ 6MPa,

https://doi.org/10.5281/zenodo.13971076

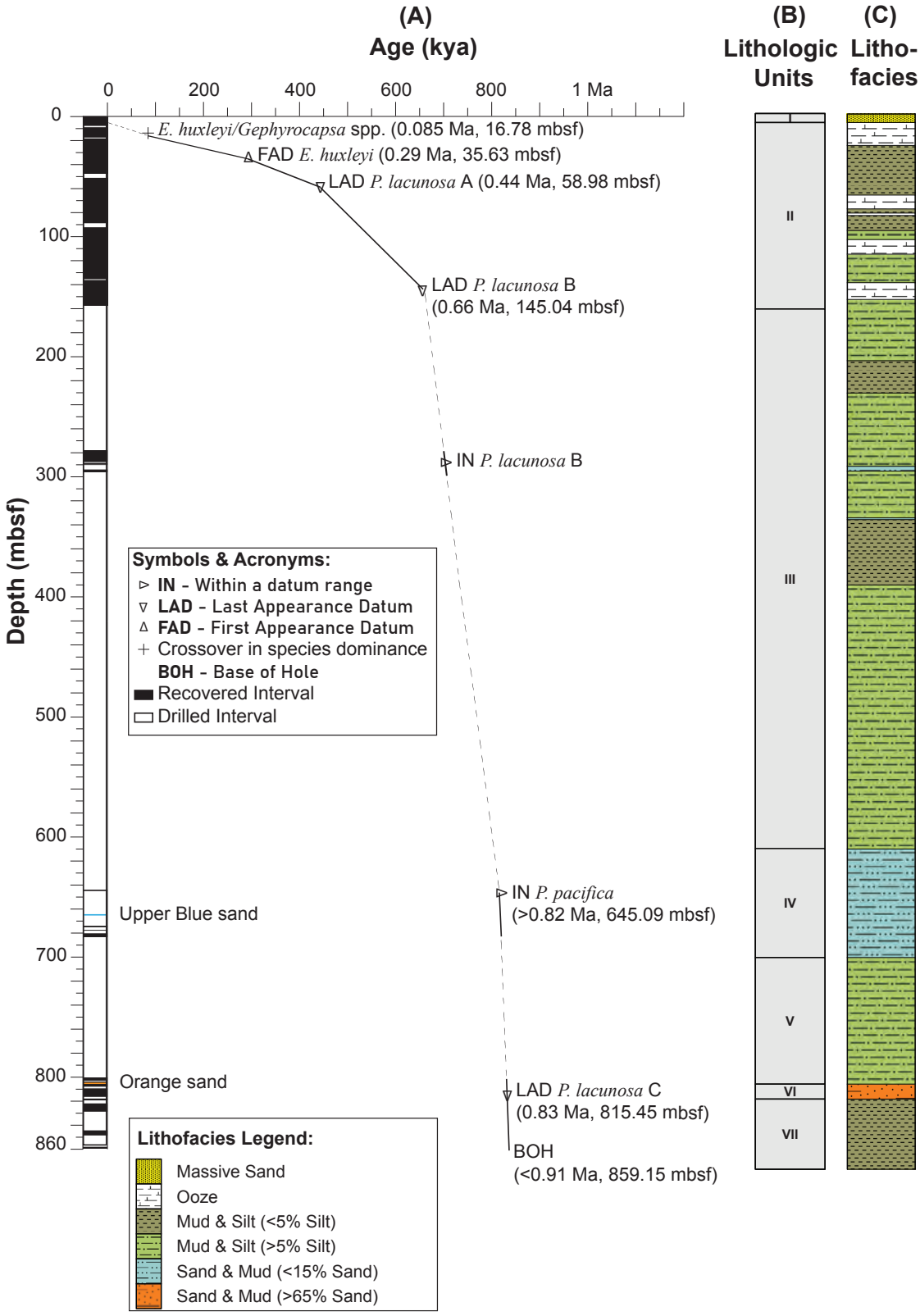

Figure F24: Composite time-depth plot of calcareous nannofossil biohorizons through Hole H003 and Hole H002 using compressed depths. Calcareous nannofossil events are from the Biostratigraphic Chart – Gulf Basin, USA (Waterman et al., **2017**), Gradstein et al. (**2012**), and Constans and Parker (**1986**). On the age-depth curve, solid black lines correlate with recovered intervals where samples were taken regularly for biostratigraphic analysis. Dashed black lines correlate with drilled intervals through which sediment samples were not recovered and biostratigraphic analysis could not be performed. First appearance datums (FAD, evolution) are shown as upright triangles, and last appearance datums (LAD, extinction) are shown as inverted triangles. All depths are compressed measured depth in meters below the seafloor (mbsf). Methods and further discussion can be found in the calcareous nannofossil biostratigraphy sections of Methods (Flemings et al., **2025b**) and Site H (Flemings et al., **2025a**).

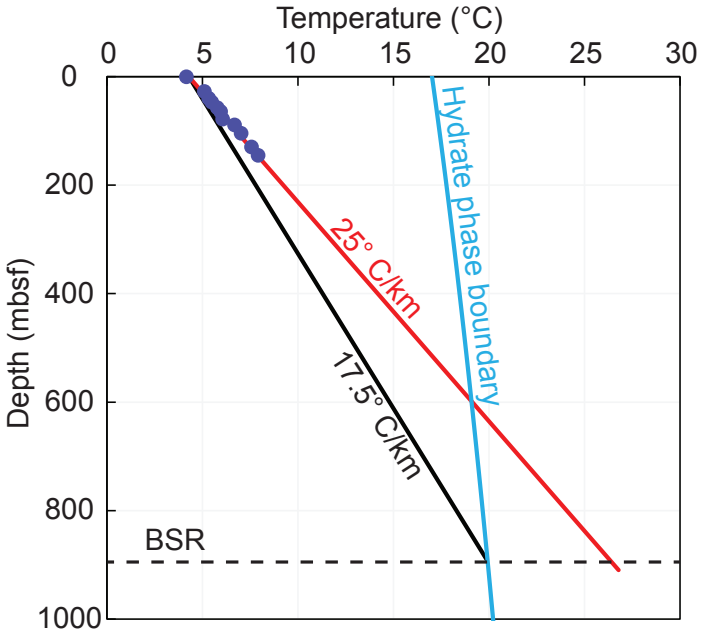

Figure F25: Temperatures with true-vertical depth in meters below the seafloor (mbsf). The gradient of 25 °C/km (red line) is linear fit using measured temperature values (blue circles). The black line is the inferred linear temperature profile by considering the intersection between the bottom simulating reflector (BSR) depth (black dashed line), the hydrate phase boundary (light blue line) and the seafloor temperature. Methods and further discussion can be found in the in-situ temperature sections of Methods (Flemings et al., **2025b**) and Site H (Flemings et al., **2025a**).

which records the dissociation of hydrate into gas and water. From this sample, 4.28 L of methane was produced from a 65 cm long section of pressure core. A similar volume of methane was produced from the 20 cm section, Section H002-02FB-4 (blue triangles), due to its higher hydrate saturation. In this case, the lower pressures are most likely due to endothermic cooling as the concentrated hydrate is dissociated.

Dissolved methane concentration increased with depth and reached 100% saturation at 146.6-147.5 mbsf (Section H003-24CS-5) (Figure **F27**, column C). Beneath this depth, hydrate was present (Figure **F27**, column D). This increase in methane concentration was coincident with a decline with depth in the total organic carbon (Figure **F27**, column E), and increase in the $\delta^{13}C$ value with depth. Taken together, these observations suggest increasing biodegradation has occurred with depth (You et al., **2019**).

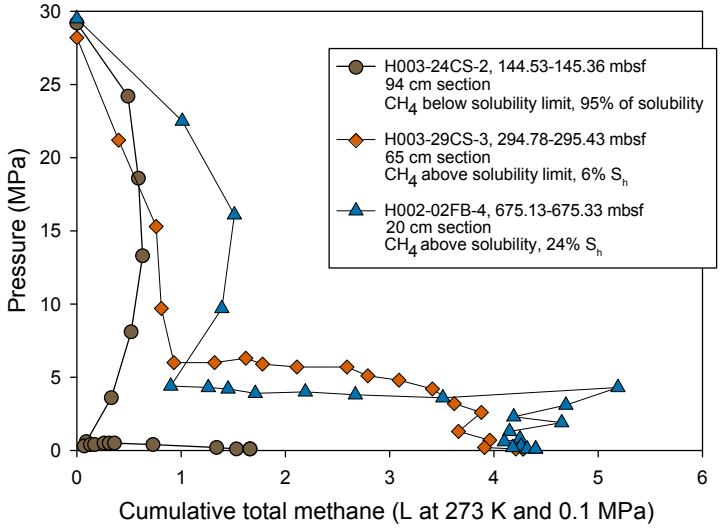

Figure F26: Example quantitative degassing results. Cumulative total volume of methane (CH_4) (including total methane expelled and remaining in the core storage chamber) produced from three sections of pressure core as pressure is decreased in steps. The brown circles show a long (94 cm) unsaturated sample (dissolved methane concentration is less than 100% and there is no hydrate, Section H003-24CS-2). The orange diamonds show a shorter (65 cm) saturated sample with a small amount of methane hydrate (dissolved methane concentration is 100% and the methane hydrate concentration was 6% of the pore space, Section H003-29CS-3). The blue triangles show and even shorter (20 cm) saturated sample with a higher concentration of methane hydrate (dissolved methane concentration is 100% and the average methane hydrate concentration in the pore space was 24%, but with most of the hydrate concentrated in the lower half (Section H002-02FB-4). Thus, the actual hydrate concentration was higher in this layer. Decreases in total methane with decreasing pore are not real but artifacts introduced when accounting for the change in volume of equipment as the pressure decreases. Methods and further discussion can be found in the dissolved gas concentrations and hydrate saturation sections of Methods (Flemings et al., **2025b**) and Site H (Flemings et al., **2025a**).

Gas geochemistry

Hydrocarbon gases produced during quantitative degassing were analyzed and found to all be > 99.99% methane. Gas samples from voids inside the core liner were extracted into syringes and gas bags. Void gases in syringes were measured onboard via gas chromatography with a thermal conductivity detector (GC-TCD) within hours of collection. Void gases could only be collected on conventional cores. Pressure core gas samples were also collected during depressurization in syringes and a subset in gas bags.

https://doi.org/10.5281/zenodo.13971076

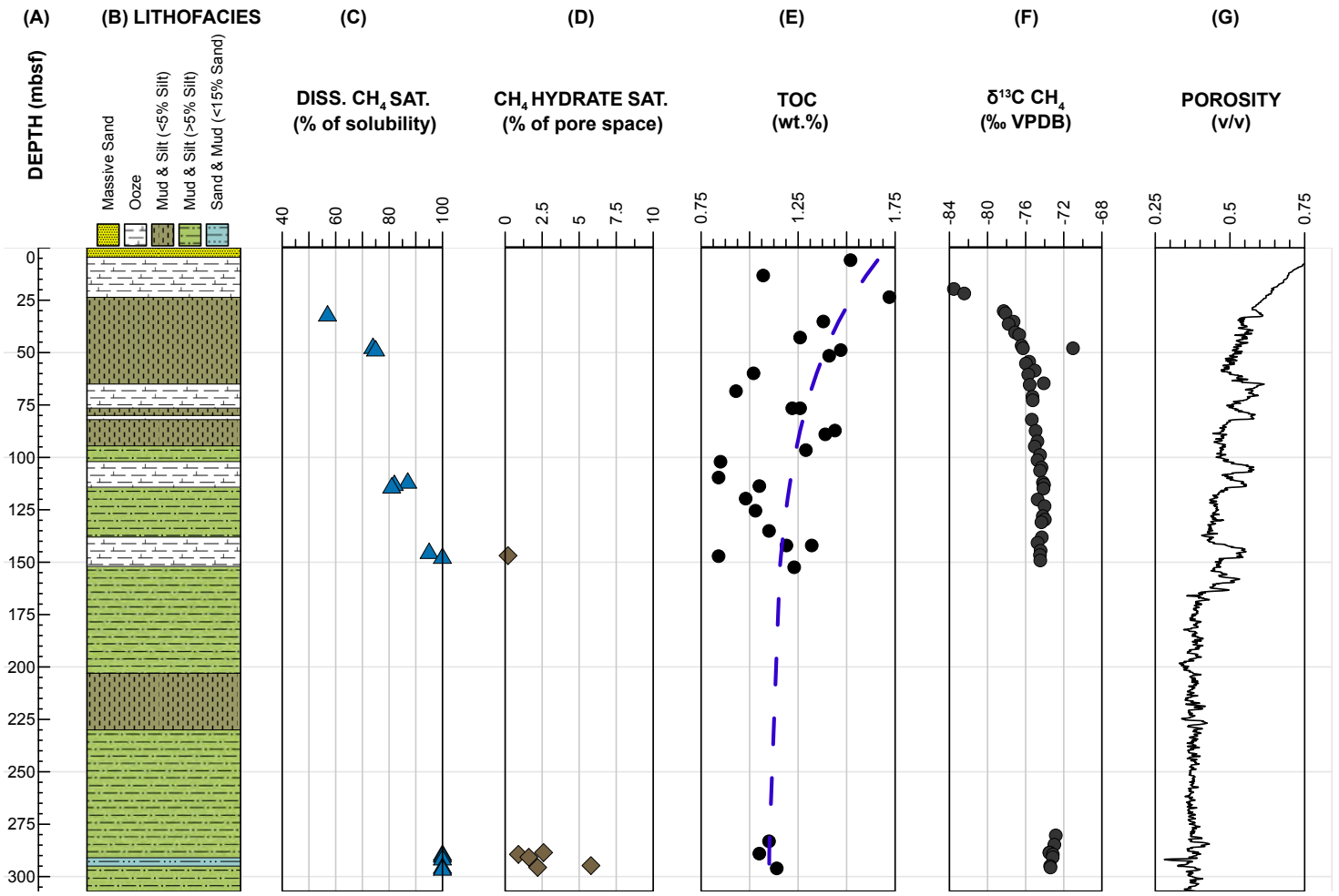

Figure F27: Concentration of methane, methane hydrate saturation, total organic carbon, carbon isotopes of methane, and porosity. A) Measured depth in meters below seafloor (mbsf); B) Lithofacies; C) Methane concentration expressed as a function of the maximum solubility of methane in pore water; D) Hydrate saturation; E) Total organic carbon (TOC). The decrease in TOC as highlighted by the dash blue line (logarithmic fit) reflects microbial consumption of TOC; F) $\delta^{13}C$ isotopes of CH_4 reported relative to the Vienna Pee Dee Belemnite (VPDB) standard; G) Projected LWD porosity derived from LWD density. The derivation is discussed in **Site H: Seismic and LWD interpretation**. The depth projection of LWD data onto Hole H002 and Hole H003 is discussed in Site H (Flemings et al., **2025a**). All depths are compressed measured depth in meters below the seafloor (mbsf). Methods and further discussion of geochemistry and index properties can be found in Methods (Flemings et al., **2025b**) and Site H (Flemings et al., **2025a**).

Methane to ethane (C_1/C_2) and methane to ethane and propane ($C_1/(C_2+C_3)$) decrease with depth, mainly driven by the increase in ethane with depth (Figure **F28**). Ethane is present only in trace amounts (9 to 114 ppm) in all samples. Most samples contain trace propane (< 9 ppm) and fewer contain i-butane or n-butane (< 4 ppm). All values of C_1/C_2 and $C_1/(C_2+C_3)$ are relatively high (>1000). $\delta^{13}C$-CH_4 (Figure **F28**, left-most column) increases with depth, but all values are lighter than -69.3 ‰ VPDB (mean: -73.9 ‰ VPDB).

The decrease in C_1/C_2 and increase in $\delta^{13}C$-CH_4 is most apparent in the continuously cored section (0-155.1 mbsf) but the values near the Red sand (~280-300 mbsf) and through the Upper Blue sand unit (~674-678 mbsf) are consistent with the overall trend of the shallower sediments. The highest variability was observed in the cores through the Orange sand interval (~800-820 mbsf). No gas samples have yet been collected from quantitative degassing of the high-saturation intervals.

Overall, the gas composition of light $\delta^{13}C$-CH_4 and high $C_1/(C_2+C_3)$ is consistent with a mainly microbial source of methane with only very minor thermogenic components. Future gas chemistry analyses will be necessary to determine the specific methanogenesis pathways, possible secondary methane generation, or the possible presence of microbial ethane.

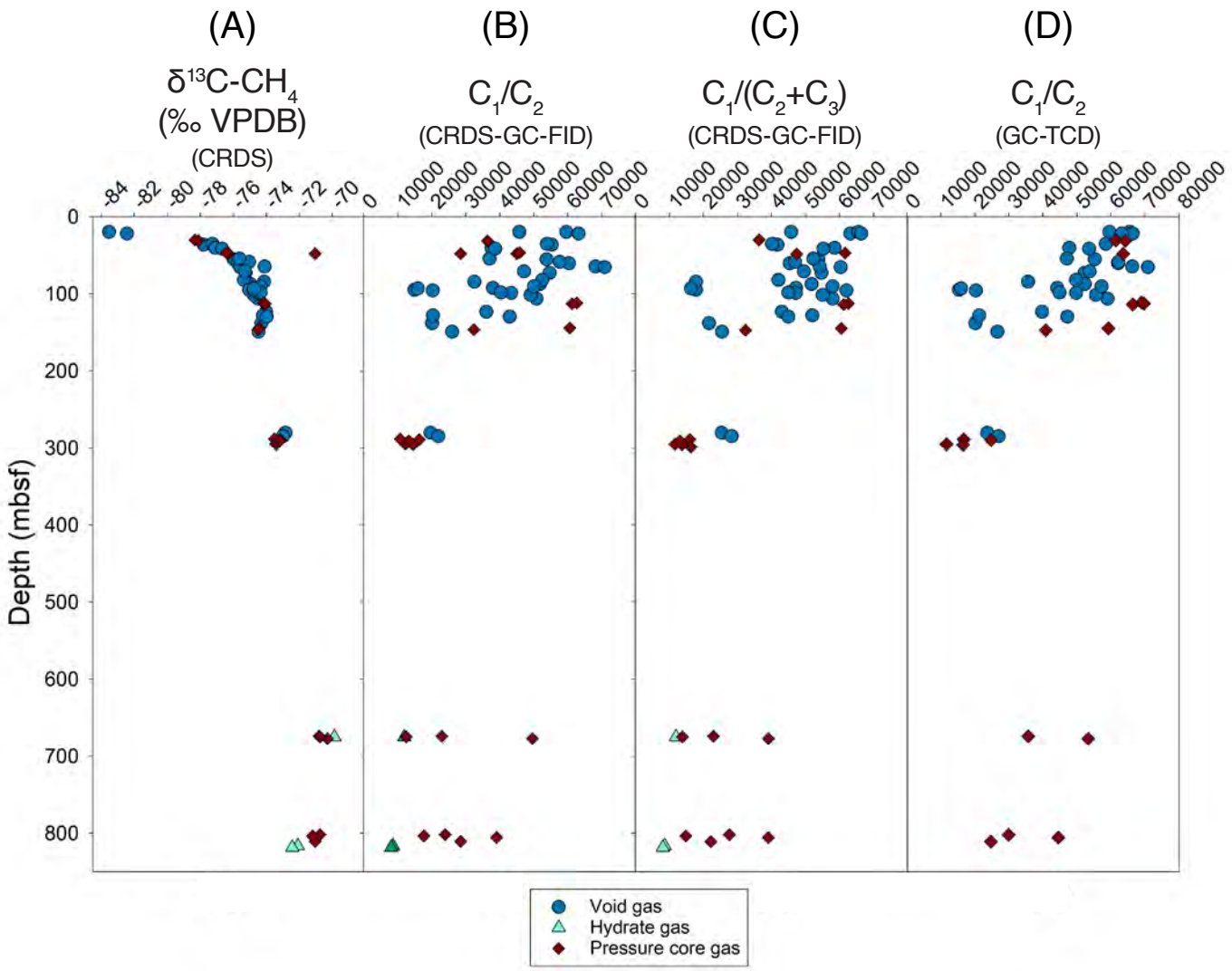

Figure F28: Carbon isotopes of methane ($\delta^{13}C$) and molecular ratios for void, pressure core, and hydrate gas samples from Site H. A) $\delta^{13}C$-CH_4 measured post-expedition using a Cavity Ring-Down Spectrometer (CRDS) and reported concentrations are relative to the Vienna Pee Dee Belemnite (VPDB) standard; B) Methane to ethane (C_1/C_2) measured post-expedition using higher-sensitivity gas chromatography with a Flame Ionization Detector (GC-FID); C) $C_1/(C_2+C_3)$ measured post-expedition using CRDS and GC-FID; D) C_1/C_2 measured onboard within hours of collection using gas chromatography with a thermal conductivity detector (GC-TCD); All depths are compressed measured depth in meters below the seafloor (mbsf). Methods and further discussion can be found in the gas geochemistry sections of Methods (Flemings et al., 2025b) and Site H (Flemings et al., 2025a).

https://doi.org/10.5281/zenodo.13971076

UT-GOM2-2 science party members enjoy the sunset while relaxing off shift on the *Q4000* helipad. Photo credit: Geotek Ltd.

Summary

Expedition UT-GOM2-2 successfully drilled and cored from the seafloor to near the base of the hydrate stability zone more than 800 meters below the seafloor. Sampling spanned from the seafloor to the base of the hydrate stability zone. In the years ahead, analysis of the data acquired from this expedition will further illuminate the dynamics of the microbial factory that drives hydrate formation and provide insight into the potential of the gas hydrate reservoir as a future energy resource.

References

Archie, G. E., 1942, The Electrical Resistivity Log as an Aid in Determining Some Reservoir Characteristics, Transactions of AIME, Volume 146, p. 4, https://doi.org/10.2118/942054-g.

Bhati, A., Kar, A., and Bahadur, V., 2024, Analysis of CO_2 hydrate formation from flue gas mixtures in a bubble column reactor: Separation and Purification Technology, v. 330, https://doi.org/10.1016/j.seppur.2023.125261.

Biastoch, A., Treude, T., Rüpke, L. H., Riebesell, U., Roth, C., Burwicz, E. B., Park, W., Latif, M., Böning, C. W., Madec, G., and Wallmann, K., 2011, Rising Arctic Ocean temperatures cause gas hydrate destabilization and ocean acidification: Geophysical Research Letters, v. 38, no. 8, p. L08602, https://doi.org/10.1029/2011GL047222.

Boswell, R., 2009, Is gas hydrate energy within reach?: Science, v. 325, no. 5943, p. 957-958, https://doi.org/10.1126/science.1175074.

Boswell, R., and Collett, T. S., 2011, Current perspectives on gas hydrate resources: Energy & Environmental Science, v. 4, no. 4, p. 1206-1215, https://doi.org/10.1039/C0EE00203H.

Boswell, R., Collett, T. S., Frye, M., Shedd, W., McConnell, D. R., and Shelander, D., 2012a, Subsurface gas hydrates in the northern Gulf of Mexico: Marine and Petroleum Geology, v. 34, no. 1, p. 4-30, https://doi.org/10.1016/j.marpetgeo.2011.10.003.

Boswell, R., Frye, M., Shelander, D., Shedd, W., McConnell, D. R., and Cook, A., 2012b, Architecture of gas-hydrate-bearing sands from Walker Ridge 313, Green Canyon 955, and Alaminos Canyon 21: Northern deepwater Gulf of Mexico: Marine and Petroleum Geology, v. 34, no. 1, p. 134-149, https://doi.org/10.1016/j.marpetgeo.2011.08.010.

Boswell, R., Shipp, C., Reichel, T., Shelander, D., Saeki, T., Frye, M., Shedd, W., Collett, T. S., and McConnell, D. R., 2016, Prospecting for marine gas hydrate resources: Interpretation, v. 4, no. 1, p. SA13-SA24, https://doi.org/10.1190/int-2015-0036.1.

Boswell, R., Schoderbek, D., Collett, T. S., Ohtsuki, S., White, M., and Anderson, B. J., 2017, The Iġnik Sikumi Field Experiment, Alaska North Slope: Design, Operations, and Implications for CO_2–CH_4 Exchange in Gas Hydrate Reservoirs: Energy & Fuels, v. 31, no. 1, p. 140-153, https://doi.org/10.1021/acs.energyfuels.6b01909.

Boswell, R., Myshakin, E., Moridis, G., Konno, Y., Collett, T. S., Reagan, M., Ajayi, T., and Seol, Y., 2019, India National Gas Hydrate Program Expedition 02 summary of scientific results: Numerical simulation of reservoir response to depressurization: Marine and Petroleum Geology, v. 108, p. 154-166, https://doi.org/10.1016/j.marpetgeo.2018.09.026.

Boudreau, B. P., Luo, Y., Meysman, F. J. R., Middelburg, J. J., and Dickens, G. R., 2015, Gas hydrate dissociation prolongs acidification of the Anthropocene oceans: Geophysical Research Letters, v. 42, no. 21, https://doi.org/10.1002/2015gl065779.

Boyer, T. P., Baranova, O. K., Coleman, C., Garcia, H. E., Grodsky, A., Locarnini, R. A., Mishonov, A. V., O'Brien, T. D., Paver, C. R., Reagan, J. R., Seidov, D., Smolyar, I. V., Weathers, K., and Zweng, M. M., 2018, World Ocean Database 2018, NOAA Atlas NESDIS 87: Silver Spring, MD, NOAA, https://doi.org/10.7289/V5NZ85MT.

BSEE, 2024, BSEE Data Center, https://www.data.bsee.gov/.

Claypool, G. E., and Kaplan, I. R., 1974, The Origin and Distribution of Methane in Marine Sediments, in Kaplan, I., ed., Natural Gases in Marine Sediments, Volume 3, Springer US, p. 99-139, https://doi.org/10.1007/978-1-4684-2757-8_8.

Collett, T. S., Boswell, R., Frye, M., Shedd, W., Godfriaux, P., Dufrene, R., McConnell, D., Mrozewski, S., Guerin, G., Cook, A., Jones, E., and Roy, R., 2009, Gulf of Mexico Gas Hydrate Joint Industry Project Leg II: Operational Summary: Proceedings of the Drilling and Scientific Results of the 2009 Gulf of Mexico Gas Hydrate Joint Industry Project Leg II, p. 27, https://netl.doe.gov/sites/default/files/netl-file/OpSum%5B1%5D.pdf.

Collett, T. S., Boswell, R., Frye, M., Shedd, W. W., Godfriaux, P. D., Dufrene, R. S., McConnell, D. R., Mrozewski, S., Guerin, G., Cook, A., Jones, E., and Roy, R., 2010, Gulf of Mexico Gas Hydrate Joint Industry Project Leg II: Logging-While-Drilling Operations and Challenges, Offshore Technology Conference, Offshore Technology Conference, https://doi.org/10.4043/20452-ms.

Collett, T. S., Lee, M. W., Zyrianova, M. V., Mrozewski, S. A., Guerin, G., Cook, A. E., and Goldberg, D. S., 2012, Gulf of Mexico Gas Hydrate Joint Industry Project Leg II logging-while-drilling data acquisition and analysis: Marine and Petroleum Geology, v. 34, no. 1, p. 41-61, https://doi.org/10.1016/j.marpetgeo.2011.08.003.

Constans, R. E., and Parker, M. E., 1986, Calcareous nannofossil biostratigraphy and paleoclimatic indices for the late Quaternary, Deep Sea Drilling Project, Leg 96, Gulf of Mexico, Initial Reports of the Deep Sea Drilling Project, 96, p. 601–630, https://doi.org/10.2973/dsdp.proc.96.132.1986.

Cook, A. E., Anderson, B. I., Malinverno, A., Mrozemski, S., and Goldberg, D. S., 2010, Electrical anisotropy due to gas hydrate-filled fractures: Geophysics, v. 75, no. 6, p. 13, https://doi.org/10.1190/1.3506530.

Cook, A. E., Anderson, B. I., Rasmus, J., Sun, K., Li, Q., Collett, T. S., and Goldberg, D. S., 2012, Electrical anisotropy of gas hydrate-bearing sand reservoirs in the Gulf of Mexico: Marine and Petroleum Geology, v. 34, no. 1, p. 72-84, https://doi.org/10.1016/j.marpetgeo.2011.09.003.

Cook, A. E., Goldberg, D. S., and Malinverno, A., 2014, Natural gas hydrates occupying fractures: A focus on non-vent sites on the Indian continental margin and the northern Gulf of Mexico: Marine and Petroleum Geology, v. 58, p. 278-291, https://doi.org/10.1016/j.marpetgeo.2014.04.013.

Cook, A. E., and Waite, W. F., 2018, Archie's Saturation Exponent for Natural Gas Hydrate in Coarse-Grained Reservoirs, v. 123, no. 3, p. 2069-2089, https://doi.org/10.1002/2017jb015138.

Darnell, K. N., Flemings, P. B., and DiCarlo, D., 2019, Nitrogen-Driven Chromatographic Separation During Gas Injection Into Hydrate-Bearing Sediments: Water Resources Research, https://doi.org/10.1029/2018wr023414.

Dickens, G. R., Wallace, P. J., Paull, C. K., and Borowski, W. S., 2000, Detection of methane gas hydrate in the pressure core sampler (PCS): volume-pressure-time relations during controlled degassing experiments: Proceedings of the Ocean Drilling Program Scientific Results, v. 164, p. 113-117, https://doi.org/10.2973/odp.proc.sr.164.210.2000.

Dickens, G. R., 2003, A Methane Trigger for Rapid Warming?: Science, v. 299, no. 5609, p. 1017-1017, https://doi.org/10.1126/science.1080789.

Diegel, F. A., Karlo, J. F., Schuster, D. C., Shoup, R. C., and Tauvers, P. R., 1995, Cenozoic structural evolution and tectono-stratigraphic framework of the northern Gulf coast continental margin, in Jackson, M. P. A., Roberts, D. G., and Snelson, S., eds., Salt tectonics: a global perspective: AAPG Memoir 65, p. 109-151, https://doi.org/10.1306/M65604C6.

Eaton, B. A., 1969, Fracture gradient prediction and its application in oil field operations: Journal of Petroleum Technology, v. 21, no. 10, p. 1353-1360, https://doi.org/10.2118/2163-PA.

Fang, Y., Flemings, P. B., Daigle, H., Phillips, S. C., Meazell, P. K., and You, K., 2020, Petrophysical properties of the Green Canyon Block 955 hydrate reservoir inferred from reconstituted sediments: Implications for hydrate formation and production: AAPG Bulletin, v. 104, no. 9, p. 1997-2028, https://doi.org/10.1306/01062019165.

Flemings, P. B., 2021, A Concise Guide to Geopressure: Origin, Prediction, and Applications, Cambridge Press, https://doi.org/10.1017/9781107326309.

Flemings, P. B., Thomas, C., Collett, T. S., Colwell, F., Cook, A. E., Germaine, J., Holland, M., Houghton, J., Johnson, J. E., Malinverno, A., Meazell, K., Pettigrew, T., Phillips, S. C., Portnov, A., Price, A., Santra, M., Schultheiss, P., Solomon, E., and You, K., 2023a, UT-GOM2-2 Prospectus: Science and Sample Distribution Plan, https://doi.org/10.5281/zenodo.13694088.

Flemings, P. B., Cook, A. E., Houghton, J., Morrison, J., Portnov, A., Pettigrew, T., Phillips, S. C., Polito, P., Santra, M., and Thomas, C., 2023b, UT-GOM2-2 Operations Plan, https://ig.utexas.edu/wp-content/uploads/2023/06/OperationsPlan_Rev2.3.pdf.

Flemings, P. B., Thomas, C., Phillips, S. C., Collett, T. S., Cook, A. E., Solomon, E., Colwell, F. S., Johnson, J. E., Awwiller, D., Aylward, I., Bhandari, A. R., Brooks, D., Buser-Young, J. Z., Cardona, A., Casso, M. A., Coyte, R., Darrah, T., Davis, M., Dugan, B., Duncan, D., Germaine, J. T., Holland, M., Houghton, J., Martin, S., Mills, N. T., Mimitz, M., Minarich, D., Morono, Y., Murphy, Z., O'Connell, J., Petrou, E., Pettigrew, T., Pohlman, J. W., Portnov, A., Phillips, M. P., Redd, T., Sawyer, D. E., Schultheiss, P., Shannon, K., Sullivan, C., Small, C., Tozier, K., Tsang, M.-Y., Maal, C. V. D., Waite, W. F., and Walton, T., 2025a, Expedition UT-GOM2-2 Site H, in Flemings, P. B., ed., Proceedings of the Deepwater Hydrate Coring Expedition UT-GOM2-2: The University of Texas as Austin, University of Texas Institute for Geophysics, https://doi.org/10.5281/zenodo.13971276.

Flemings, P. B., Thomas, C., Phillips, S. C., Collett, T. S., Cook, A. E., Solomon, E., Colwell, F. S., Johnson, J. E., Awwiller, D., Aylward, I., Bhandari, A. R., Brooks, D., Buser-Young, J. Z., Cardona, A., Casso, M. A., Coyte, R., Darrah, T., Davis, M., Dugan, B., Duncan, D., Germaine, J. T., Holland, M., Houghton, J., Martin, S., Mills, N. T., Mimitz, M., Minarich, D., Morono, Y., Murphy, Z., O'Connell, J., Petrou, E., Pettigrew, T., Pohlman, J. W., Portnov, A., Phillips, M. P., Redd, T., Sawyer, D. E., Schultheiss, P., Shannon, K., Sullivan, C., Small, C., Tozier, K., Tsang, M.-Y., Maal, C. V. D., Waite, W. F., and Walton, T., 2025b, Expedition UT-GOM2-2 Methods, in Flemings, P. B., ed., Proceedings of the Deepwater Hydrate Coring Expedition UT-GOM2-2: The University of Texas as Austin, University of Texas Institute for Geophysics, https://doi.org/10.5281/zenodo.13971228.

Fofonoff, N., and Millard, R., 1983, Algorithms for Computation of Fundamental Properties of Seawater: UNESCO Tech. Pap. Mar. Sci., v. 44, https://doi.org/10.25607/OBP-1450.

Frye, M., Shedd, W., and Boswell, R., 2012, Gas hydrate resource potential in the Terrebonne Basin, Northern Gulf of Mexico: Marine and Petroleum Geology, v. 34, no. 1, p. 150-168, https://doi.org/10.1016/j.marpetgeo.2011.08.001.

Goldberg, D. S., Kleinberg, R. L., Weinberger, J. L., Malinverno, A., McLellan, P. J., and Collett, T. S., 2010, 16. Evaluation of Natural Gas-Hydrate Systems Using Borehole Logs, Geophysical Characterization of Gas Hydrates, p. 239-261, https://doi.org/10.1190/1.9781560802197.ch16.

Gradstein, F. M., Ogg, J. G., Schmitz, M. D., and Ogg, G. M., 2012, Geologic Time Scale 2012 -- 2 volume book, **https://www.sciencedirect.com/book/9780444594259/the-geologic-time-scale**.

Hillman, J. I. T., Cook, A. E., Daigle, H., Nole, M., Malinverno, A., Meazell, K., and Flemings, P. B., 2017a, Gas hydrate reservoirs and gas migration mechanisms in the Terrebonne Basin, Gulf of Mexico: Marine and Petroleum Geology, v. 86, p. 1357-1373, **https://doi.org/10.1016/j.marpetgeo.2017.07.029**.

Hillman, J. I. T., Cook, A. E., Sawyer, D. E., Küçük, H. M., and Goldberg, D. S., 2017b, The character and amplitude of 'discontinuous' bottom-simulating reflections in marine seismic data: Earth and Planetary Science Letters, v. 459, p. 157-169, **https://doi.org/10.1016/j.epsl.2016.10.058**.

Hutchinson, D. R., Shelander, D., Dai, J., McConnell, D., Shedd, W., Frye, M., Ruppel, C., Boswell, R., Jones, E., Collett, T., Rose, K., Dugan, B., Wood, W., and Latham, T., Site Selection for DOE/JIP Gas Hydrate Drilling in the Northern Gulf of Mexico, in Proceedings 6th International Conference on Gas Hydrates (ICGH 2008), Vancouver, British Columbia, Canada, July 6-10, **https://netl.doe.gov/sites/default/files/2018-12/ICGH_5506_1_41330_0.pdf**.

Isson, T. T., Planavsky, N. J., Coogan, L. A., Stewart, E. M., Ague, J. J., Bolton, E. W., Zhang, S., McKenzie, N. R., and Kump, L. R., 2020, Evolution of the Global Carbon Cycle and Climate Regulation on Earth: Global Biogeochemical Cycles, v. 34, no. 2, p. e2018GB006061, **https://doi.org/10.1029/2018GB006061**.

Kayen, R. E., and Lee, H. J., 1991, Pleistocene slope instability of gas hydrate-laden sediment on the Beaufort margin: Marine Geotechnology, v. 10, **https://doi.org/10.1080/10641199109379886**.

Kennett, J. P., Cannariato, K. G., Hendy, I. L., and Behl, R. J., 2000, Carbon Isotopic Evidence for Methane Hydrate Instability During Quaternary Interstadials: Science, v. 288, no. 5463, p. 128-133, **https://doi.org/10.1126/science.288.5463.128**.

Kramer, K., and Shedd, W., 2017, A 1.4-Billion-Pixel Map of the Gulf of Mexico Seafloor: Eos, **https://doi.org/10.1029/2017EO073557**.

Kumar, A., Cook, A., and UT-GOM2-2 Scientists, An Unusual Seafloor Sand in the Terrebonne Basin, Gulf of Mexico, in Proceedings AGU Fall Meeting, Volume 2024, **https://agu.confex.com/agu/agu24/meetingapp.cgi/Paper/1682070**.

Kvenvolden, K. A., 1988, Methane Hydrate: A Major Reservoir of Carbon in the Shallow Geosphere?: Chemical Geology, v. 71, p. 11, **https://doi.org/10.1016/0009-2541(88)90104-0**.

Kvenvolden, K. A., 2012, Methane hydrates and global climate: Global Biogeochemical Cycles, v. 2, no. 3, p. 221-229, **https://doi.org/10.1029/GB002i003p00221**.

Malinverno, A., and Goldberg, D. S., 2015, Testing short-range migration of microbial methane as a hydrate formation mechanism: Results from Andaman Sea and Kumano Basin drill sites and global implications: Earth and Planetary Science Letters, v. 422, p. 105-114, **https://doi.org/10.1016/j.epsl.2015.04.019**.

McConnell, D., and Zhang, Z., 2005, Using acoustic inversion to image buried gas hydrate distribution: Fire in the Ice, v. 5, no. 4, p. 3-5, **https://netl.doe.gov/sites/default/files/publication/HMNewsFall05_HighRez.pdf**.

McConnell, D. R., and Kendall, B. A., 2002, Images of the Base of Gas Hydrate Stability, Northwest Walker Ridge, Gulf of Mexico, Offshore Technology Conference: Houston, Texas, **https://doi.org/10.4043/14103-ms**.

Meazell, P. K., and Flemings, P. B., 2022, The evolution of seafloor venting from hydrate-sealed gas reservoirs: Earth and Planetary Science Letters, v. 579, p. 13, **https://doi.org/10.1016/j.epsl.2021.117336**.

Mienert, J., Vanneste, M., Bünz, S., Andreassen, K., Haflidason, H., and Sejrup, H. P., 2005, Ocean warming and gas hydrate stability on the mid-Norwegian margin at the Storegga Slide: Marine and Petroleum Geology, v. 22, no. 1-2, p. 233-244, **https://doi.org/10.1016/j.marpetgeo.2004.10.018**.

Milkov, A. V., 2004, Global estimates of hydrate-bound gas in marine sediments: how much is really out there?: Earth-Science Reviews, v. 66, no. 3–4, p. 183-197, **https://doi.org/10.1016/j.earscirev.2003.11.002**.

Moridis, G., Kowalsky, M. B., and Pruess, K., 2012, TOUGH+HYDRATE v1.2 User's Manual: A Code for the Simulation of System Behavior in Hydrate-Bearing Geologic Media, Lawrence Berkeley National Laboratory, **https://escholarship.org/uc/item/3mk82656**.

Portnov, A., Flemings, P. B., You, K., Meazell, K., Hudec, M. R., and Dunlap, D. B., 2023, Low temperature and high pressure dramatically thicken the gas hydrate stability zone in rapidly formed sedimentary basins: Marine and Petroleum Geology, v. 158, p. 106550, **https://doi.org/10.1016/j.marpetgeo.2023.106550**.

Prather, B. E., Booth, J. R., Steffens, G. S., and Craig, P. A., 1998, Classification, lithologic calibration, and stratigraphic succession of seismic facies of intraslope basins, deep-water Gulf of Mexico: AAPG Bulletin, v. 82, no. 5, p. 701-728, **https://doi.org/10.1306/1D9BC5D9-172D-11D7-8645000102C1865D**.

Reeburgh, W. S., 2007, Oceanic methane biogeochemistry: Chem. Rev., v. 107, p. 486-513, https://doi.org/10.1021/cr050362v.

Ruppel, C. D., and Kessler, J. D., 2017, The interaction of climate change and methane hydrates: Reviews of Geophysics, v. 55, no. 1, p. 126-168, https://doi.org/10.1002/2016RG000534.

Schuur, E. A. G., Bockheim, J., Canadell, J. G., Euskirchen, E., Field, C. B., Goryachkin, S. V., Hagemann, S., Kuhry, P., Lafleur, P. M., Lee, H., Mazhitova, G., Nelson, F. E., Rinke, A., Romanovsky, V. E., Shiklomanov, N., Tarnocai, C., Venevsky, S., Vogel, J. G., and Zimov, S. A., 2008, Vulnerability of Permafrost Carbon to Climate Change: Implications for the Global Carbon Cycle: BioScience, v. 58, no. 8, p. 701-714, https://doi.org/10.1641/b580807.

Shedd, W., Frye, M., Godfriaux, P., Dufrene, R., McConnell, D., Boswell, R., Collett, T., Mrozewski, S., Guerin, G., Cook, A., Shelander, D., and Dai, J., 2010, Gulf of Mexico Gas Hydrates Joint Industry Project Leg II: Results from the Walker Ridge 313 Site, Offshore Technology Conference, https://doi.org/10.4043/20806-MS.

Shedd, W., Boswell, R., Frye, M., Godfriaux, P., and Kramer, K., 2012, Occurrence and nature of "bottom simulating reflectors" in the northern Gulf of Mexico: Marine and Petroleum Geology, v. 34, no. 1, p. 31-40, https://doi.org/10.1016/j.marpetgeo.2011.08.005.

Sloan, E. D., and Koh, C. A., 2007, Clathrate Hydrates of Natural Gases, Boca Raton, FL, CRC Press, https://doi.org/10.1201/9781420008494.

Tsuji, Y., Ishida, H., Nakamizu, M., Matsumoto, R., and Shimizu, S., 2004, Overview of the MITI Nankai Trough Wells: A Milestone in the Evaluation of Methane Hydrate Resources, v. 54, no. 1, p. 3-10, https://doi.org/10.1111/j.1751-3928.2004.tb00182.x.

Varona, G. M., Flemings, P. B., and Portnov, A., 2023, Hydrate-bearing sands record the transition from ponded deposition to bypass in the deep-water Gulf of Mexico.: Marine and Petroleum Geology, v. 151, no. JMPG_106172, https://doi.org/10.1016/j.marpetgeo.2023.106172.

Waterman, A. S., Weber, R. D., Lu, Y., Smith, V. E., George, R. A., Reilly, T. M., Roederer, R. V., Edmunds, J. A., Parker, B. W., Myers, N. R., and Avery, A. J., 2017, Biostratigraphic Chart - Gulf Basin, USA, Quaternary and Neogene: Paleo-Data, Inc., https://www.paleodata.com/chart/.

Wei, L., Malinverno, A., Colwell, F., and Goldberg, D. S., 2024, Reactive transport modeling of organic carbon degradation in marine methane hydrate systems: Scientific Reports, v. 14, no. 1, p. 2837, https://doi.org/10.1038/s41598-024-52957-w.

Yin, Z., and Linga, P., 2019, Methane hydrates: A future clean energy resource: Chinese Journal of Chemical Engineering, https://doi.org/10.1016/j.cjche.2019.01.005.

You, K., Flemings, P. B., Malinverno, A., Collett, T. S., and Darnell, K., 2019, Mechanisms of Methane Hydrate Formation in Geological Systems: Reviews of Geophysics, v. 57, no. 4, p. 1146-1196, https://doi.org/10.1029/2018rg000638.

You, K., Summa, L., Flemings, P. B., Santra, M., and Fang, Y., 2021, Three-Dimensional Free Gas Flow Focuses Basin-Wide Microbial Methane to Concentrated Methane Hydrate Reservoirs in Geological System: Journal of Geophysical Research: Solid Earth, v. 126, no. 12, p. e2021JB022793, https://doi.org/10.1029/2021JB022793.

You, K., and Flemings, P. B., 2021, Methane Hydrate Formation and Evolution During Sedimentation: Journal of Geophysical Research-Solid Earth, v. 126, no. 4, https://doi.org/10.1029/2020JB021235.

Zhang, K., Moridis, G., and Pruess, K., 2011, TOUGH+CO_2: A multiphase fluid-flow simulator for CO_2 geologic sequestration in saline aquifers: Computers & Geosciences, v. 37, no. 6, p. 714-723, https://doi.org/10.1016/j.cageo.2010.09.011.

Zheng, J., Chong, Z. R., Qureshi, M. F., and Linga, P., 2020, Carbon Dioxide Sequestration via Gas Hydrates: A Potential Pathway toward Decarbonization: Energy & Fuels, v. 34, no. 9, p. 10529-10546, https://doi.org/10.1021/acs.energyfuels.0c02309.

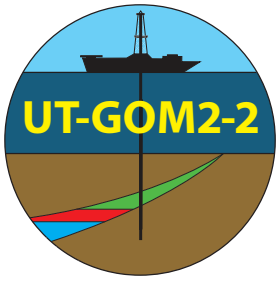

Expedition UT-GOM2-2 Summary

Proceedings of the UT-GOM2-2 Deepwater Hydrate Coring Expedition

Terrebonne Basin (Walker Ridge Block 313)

WR313 H002 (API 608124014800) and WR313 H003 (API 608124014900)

July 30–September 28, 2023 | Expedition UT-GOM2-2 Scientists

University of Texas Institute for Geophysics | 2025

https://doi.org/10.5281/zenodo.13971076